NASA
Technical
Paper
2472
C.2
December 1985

Analytical Study of Acoustic Response of a Semireverberant Enclosure With Application to Active Noise Control

Tony L. Parrott,
David B. Schein,
and Doreen Gridley

NASA

NASA Technical Paper 2472

1985

Analytical Study of Acoustic Response of a Semireverberant Enclosure With Application to Active Noise Control

Tony L. Parrott
Langley Research Center
Hampton, Virginia

David B. Schein
The George Washington University
Joint Institute for Advancement of Flight Sciences
Hampton, Virginia

Doreen Gridley
U.S. Naval Avionics Center
Indianapolis, Indiana

NASA
National Aeronautics and Space Administration

Scientific and Technical Information Branch

Summary

The acoustic response of a semireverberant enclosure with two interacting, velocity-prescribed source distributions was analyzed using standard modal analysis techniques with a view toward a better understanding of active noise control. Different source and enclosure dimensions, source separations, and single-wall admittances were studied over representative frequency bandwidths of 10 Hz with source relative phase as a parameter. Results indicate that power radiated into the enclosure agrees qualitatively with the spatial average of the mean square pressure, even though the reverberant field is nondiffuse. Decreases in acoustic power can therefore be used to estimate global noise reduction in a nondiffuse semireverberant environment. As might be expected, parametric studies indicate that maximum power reductions of up to 25 dB can be achieved when secondary and primary sources are compact and closely spaced. Although less success is achieved with increasing frequency and source separation or size, significant suppression of up to 8 dB still occurs over the 1 to 2 Hz bandwidth.

Introduction

Concern about high levels of low-frequency interior cabin noise for proposed advanced turboprop aircraft and recent developments in microprocessor control technology has stimulated new interest in active suppression of aircraft interior cabin noise. If active suppression is effective for interior cabin noise, then bulky passive absorbers or heavy barrier-type materials can be avoided, and weight can be reduced. The success of active suppression has been limited in three-dimensional acoustic spaces. Nevertheless, the modest success to date offers hope that substantial improvement may be obtained with currently available control technology through a better understanding of interactions between acoustic sources in a semireverberant environment. To realize the potential improvement, additional analytical work is required which should provide an understanding of the phenomenon involved. An overview of previous experimental and analytical work is given in references 1 and 2. This earlier work is summarized in the paragraphs which follow.

For the most part, past work on active suppression has been concentrated on one-dimensional systems. After Lueg demonstrated in 1934 that suppressions up to 25 dB can be achieved in a duct using a monopole control source (ref. 1), other workers, notably Jessel and Swinbanks, investigated more complex control-source configurations such as dipoles and tripoles in an attempt to improve system stability and bandwidth. These efforts indicate that, in principle, significant active suppression over useful bandwidths can be achieved. With the recent emergence of microprocessor-controlled adaptive control systems, it appears that practical, active suppression for one-dimensional systems will be available in the present decade.

The literature on active suppression for two- and three-dimensional acoustic spaces is sparse. In 1956, Conover (ref. 3) reported results of an attempt to suppress far-field radiation from a 15 000-kVA transformer. He achieved suppression of 6 to 25 dB over a polar angle of about 23° and out to a radial distance of 125 ft by mounting a single control source (loudspeaker) on the side of the transformer structure. Beyond the 23°, no suppression was observed for regions where the original noise level was relatively high. In regions where the original noise level was low, the levels were enhanced. Another experiment on active suppression applied to transformer noise is reported in reference 4. In this experiment, noise reductions obtained at six positions inside an office (control space) located across a courtyard from a twin-transformer installation were measured. As in the Conover experiment, a single control source was located in the vicinity of the transformers. However, the experiment differed from the others in that buildings either flanked or obstructed the direct transmission path to the control space. At the transformer fundamental frequency of 100 Hz, no less than a 6-dB reduction was observed throughout the office; in some locations, up to a 25-dB reduction was observed. At the second and third harmonics, reductions of up to 10 dB were localized to volumes of 3-ft radii or less.

The results reported by Conover (ref. 3) and Ross (ref. 4) are encouraging, because noise reductions were achieved in three-dimensional acoustic spaces of practical interest in which offending sources were noncompact. Reductions decreased and became more localized with increasing frequency, as would be expected for a single control source in the presence of an extended or noncompact source. However, multiple control sources, together with precision control of phase and amplitude may help compensate for decreasing compactness with increasing frequency.

Recently, an active control experiment was conducted by Zalas and Tichy (ref. 5) on a fully outfitted, modern turboprop aircraft. The main thrust of this experiment was to demonstrate that significant broadband control can be obtained in the vicinity of a control sensor located in an aircraft cabin. A single control source was used and the aircraft was operated at cruise conditions. Overall engine harmonic levels at the control microphone were reduced

by up to about 23 dB at frequencies ranging from 50 to 500 Hz. However, the volume extent of the reduction was disappointing. Detailed intensity mapping at the fuselage walls indicated the presence of acoustically noncompact sources of energy inflow and outflow which changed location with frequency.

The experiment described in the preceding paragraph and other recent work suggest that successful active suppression in a three-dimensional acoustic environment generated by noncompact acoustic sources requires judiciously located multiple control sources. Also, a real-time adaptive control system capable of optimizing relative phasing and amplitudes using data from multiple control sensors is necessary. The acoustic interactions between the sources and environment are sufficiently complex that experimental work cannot adequately explore all parameters of interest. Analytical guidance would therefore be of great use in ascertaining those parameters of greatest importance.

Using modal analysis, the interaction of two sources radiating into an absorptive enclosure was investigated. The parameters used were source and enclosure size, source separation and relative phase, and wall admittance. This study is an attempt to identify the relative importance of these parameters without addressing the transient behavior of the acoustic system.

Symbols

$A_1, A_2, A_3, A, B_1, B_2, B_3, B$	arbitrary constants
a	source width
b	source half-height
c	speed of sound
d	center-to-center source separation distance
f	frequency
$f_{\ell,m,n}$	resonant frequency of (ℓ, m, n) mode
$G_{m,n}$	mode coupling coefficient
i	$= \sqrt{-1}$
$K_{m,n}$	nondimensional propagation constant, $k_{m,n}/k$
$K_{m,n}^{(r)}, K_{m,n}^{(i)}$	real and imaginary parts of propagation constant
k	free-space wave number, ω/c
$k_{m,n}$	propagation constant
k_x, k_y, k_z	separation constants
L_x, L_y, L_z	enclosure dimensions
ℓ, m, n	integers
$\Delta N/\Delta f$	modal density
$P_{m,n}$	pressure associated with (m, n) mode
$p(x, y, z, t)$	acoustic field pressure
$R_{m,n}$	reflection factor associated with (m, n) mode
$T(t)$	solution of separated differential equation for time
t	time
U	prescribed source velocity
$U_{m,n}$	particle velocity associated with (m, n) mode
U_0	primary-source velocity amplitude
$u(x, y, z, t)$	acoustic particle velocity
$W_{m,n}$	power radiated in the (m, n) mode
W_t	total power radiated by source configuration
$X(x), Y(y), Z(z)$	solutions of separated differential equations for spatial dimensions
x, y, z	spatial coordinates
α	normalized source separation parameter
β	normalized admittance
$\beta^{(r)}, \beta^{(i)}$	real and imaginary parts of normalized admittance
Γ	ratio of secondary to primary source velocity, Φ_s/Φ_p
∇^2	Laplacian operator
κ	ratio of source width to enclosure width, a/L_z
$\lambda_{m,n}$	constant defined in text
μ_1, μ_2	enclosure width and height to length ratios, respectively
ν	ratio of source half-height to enclosure height, b/L_y

ξ, η, ς	nondimensional spatial coordinates, x/L_x, y/L_y, and z/L_z, respectively
ρ	density of air
Φ_p, Φ_s	primary and secondary source velocity distributions
ϕ	phase difference
$\psi_{m.n}$	reflection-factor phase angle
ω	angular frequency, kc

Superscripts:

(i)	denotes imaginary part
(r)	denotes real part
$*$	complex conjugate

A bar over a symbol denotes a spatial value. Angle brackets ($\langle\ \rangle$) denote a time average.

Analysis

The rectangular geometry depicted in figure 1(a) was chosen as a basis for the analytical model. The model consisted of a three-dimensional rectangular enclosure with two velocity sources on one wall– a primary or "offending" source and a secondary or "control" source, radiating toward an absorptive soft wall of uniform admittance. The acoustic behavior of the enclosure was investigated by using standard modal theory as given for acoustical systems in reference 6. The main physical quantity of interest was the power delivered to the absorbing wall as a function of frequency. Source separation, amplitude, relative phase, geometric dimensions, and wall admittance were treated as parameters. Also, the relationship between the power developed by the sources and the spatial average of the time-averaged or mean-square pressure was investigated.

Solution of Wave Equation

The acoustic field inside the enclosure is satisfied by the homogeneous wave equation

$$\nabla^2 p - \frac{1}{c^2}\frac{\partial^2 p}{\partial t^2} = 0 \tag{1}$$

subject to boundary conditions imposed at the wall surfaces and the prescribed source velocity distribution. A separation-of-variables solution is made with the assumption that the pressure can be written as

$$p(x, y, z, t) = X(x)\ Y(y)\ Z(z)\ T(t) \tag{2}$$

Substituting this expression into equation (1) gives

$$\frac{X''}{X} + \frac{Y''}{Y} + \frac{Z''}{Z} - \frac{1}{c^2}\frac{T''}{T} = 0 \tag{3}$$

Splitting off the time variable and equating the resulting equations to an arbitrary constant, $-k^2$ gives

$$\frac{X''}{X} + \frac{Y''}{Y} + \frac{Z''}{Z} = -k^2 \tag{4}$$

and

$$\frac{1}{c^2}\frac{T''}{T} = -k^2 \tag{5}$$

The time dependence is determined by a second-order, ordinary differential equation given by

$$T'' + (kc)^2 T = 0 \tag{6}$$

with the general solution

$$T = A\exp(ikct) + B\exp(-ikct) \tag{7}$$

Since only steady-state solutions are of interest, one of the preceding arbitrary constants can be zero. In this study, the constant A is chosen to be zero, so

$$T = B\exp(-ikct) = B\exp(-i\omega t) \tag{8}$$

where the excitation frequency ω has been introduced. Splitting off the x-dependence in equation (4) gives

$$\frac{Y''}{Y} + \frac{Z''}{Z} = -k^2 - \frac{X''}{X} = -k^2 + k_x^2 \tag{9}$$

Therefore, the differential equation for the x-dependence is

$$X'' + k_x^2 X = 0 \tag{10}$$

for which the general solution is

$$X = A_1\exp(ik_x x) + B_1\exp(-ik_x x) \tag{11}$$

Similarly, a choice of separation constants k_y^2 and k_z^2 for the y- and z-dependencies provides the equations

$$Y'' + k_y^2 Y = 0 \tag{12a}$$

$$Z'' + k_y^2 Z = 0 \tag{12b}$$

with solutions

$$Y = A_2\cos(k_y y) + B_2\sin(k_y y) \tag{13a}$$

$$Z = A_3\cos(k_z z) + B_3\sin(k_z z) \tag{13b}$$

Finally, the three separation constants are related such that

$$k^2 = k_x^2 + k_y^2 + k_z^2 \tag{14}$$

The normal component of the acoustic particle velocity at the rigid wall boundaries must be zero: it follows via the linearized momentum equation that

$$\left.\frac{\partial p}{\partial y}\right|_{y=0} = \left.\frac{\partial p}{\partial y}\right|_{y=L_y} = \left.\frac{\partial p}{\partial z}\right|_{z=0} \left.\frac{\partial p}{\partial z}\right|_{z=L_z} = 0 \tag{15}$$

When these boundary conditions are applied to the general solutions given by equation (13b), the eigenfunctions for the y- and z-directions are given by

$$Y = A_2 \cos(k_y y) \tag{16a}$$

$$Z = A_3 \cos(k_z z) \tag{16b}$$

and the eigenvalues for k_y and k_z are given by

$$k_y = \frac{m\pi}{L_y} \tag{17a}$$

$$k_z = \frac{n\pi}{L_z} \tag{17b}$$

Equation (14) can now be solved for the remaining separation constant k_x to give

$$K_{m,n} = \frac{k_x}{k} = \pm\sqrt{1 - \left(\frac{m\pi}{kL_y}\right)^2 - \left(\frac{n\pi}{kL_z}\right)^2} \tag{18}$$

where the nondimensional parameter $K_{m,n}$ has been introduced. This parameter can be interpreted as a nondimensional propagation constant for the (m,n) mode of the enclosure when viewed as a transmission duct.

In subsequent sections of this report, $K_{m,n}$ is correlated with the eigenvalues $K_{\ell,m,n}$ for the corresponding rigid wall enclosure, which can also be written in nondimensional form as

$$K_{\ell,m,n} = \frac{k_{\ell,m,n}}{k} \pm \sqrt{\left(\frac{\ell\pi}{kL_x}\right)^2 + \left(\frac{m\pi}{kL_y}\right)^2 + \left(\frac{n\pi}{kL_z}\right)^2} \tag{19}$$

The modal resonant frequencies of the rigid wall enclosure are given by

$$f_{\ell,m,n} = \frac{c}{2\pi} k K_{\ell,m,n} \tag{20}$$

The modal density for the case with the rigid wall enclosure is given by equation (9.5.12) of reference 6 as follows:

$$\frac{\Delta N}{\Delta f} \approx \frac{4\pi f^2 L_x L_y L_z}{c^3} + \frac{2\pi f(L_x L_y + L_x L_z + L_y L_z)}{2c^2} + \frac{4(L_x + L_y + L_z)}{8c} \tag{21}$$

This formula can be restated for geometrically similar enclosures as a function of the dimensionless parameters kL_x (alternatively kL_y or kL_z):

$$\frac{\Delta N}{\Delta f} \approx \left[\frac{\mu_1\mu_2}{\pi}(kL_x)^3 + \frac{(\mu_1 + \mu_2 + \mu_1\mu_2)}{2}(kL_x)^2 + \frac{(1 + \mu_1 + \mu_2)}{2}(kL_x)\right]\frac{1}{kc} \tag{22}$$

where $\mu_1 = L_y/L_x$ and $\mu_2 = L_z/L_x$. Clearly, the modal density of such enclosures does not scale linearly with $kL_x(kL_y, kL_z)$. This observation implies that enclosure size effects cannot be characterized solely on the basis of a dimensionless frequency parameter.

Modal Pressure Solution

Combining the various component solutions given by equations (8), (11), (16a), and (16b) and absorbing the arbitrary constants into $G_{m,n}$ and $R_{m,n}$, gives

$$P_{m,n} = G_{m,n} \cos\left(\frac{m\pi y}{L_y}\right) \cos\left(\frac{n\pi z}{L_z}\right) [\exp(iK_{m,n}kx) + R_{m,n}\exp(-iK_{m,n}kx)]\exp(-i\omega t) \tag{23}$$

for the pressure in the (m,n) mode. The component solutions have been assembled in such manner as to allow the enclosure to be interpreted as a transmission duct. (See ref. (7).) The $G_{m,n}$ is a coupling coefficient that quantifies source coupling into the (m,n) mode of the enclosure. The $R_{m,n}$ is a mode reflection coefficient that specifies the relative amplitude of the reflected (m,n) mode traveling in the negative x-direction. The $R_{m,n}$ and the $G_{m,n}$ coefficients must now be determined.

The axial particle velocity follows from the x-direction momentum equation to give

$$U_{m,n} = \frac{1}{ik\rho c}\frac{\partial P_{m,n}}{\partial x} \tag{24}$$

for harmonic time dependence. Therefore,

$$U_{m,n} = \frac{K_{m,n}}{\rho c} G_{m,n} \cos(m\pi\eta)\cos(n\pi\zeta) \times [\exp(ikL_x K_{m,n}\xi) - R_{m,n}\exp(-ikL_x K_{m,n}\xi)] \tag{25}$$

where the nondimensional variables $\xi = x/L_x$, $\eta = y/L_y$, and $\varsigma = z/L_z$ have been introduced. Since the admittance at the absorbing wall is spatially uniform, there is no modal coupling upon reflection. (See ref. 6, section 9.3.) Therefore, the normalized admittance presented to each (m, n) mode is defined by

$$\beta = \rho c \left. \frac{U_{m,n}}{P_{m,n}} \right|_{\xi=1} \tag{26}$$

Thus,

$$\frac{U_{m,n}}{P_{m,n}} = \frac{K_{m,n}}{\rho c} \left[\frac{\exp(iK_{m,n}kL_x) - R_{m,n}\exp(-iK_{m,n}kL_x)}{\exp(iK_{m,n}kL_x) + R_{m,n}\exp(-iK_{m,n}kL_x)} \right] \tag{27}$$

Solving for $R_{m,n}$ yields

$$R_{m,n} = \frac{K_{m,n} - \beta}{K_{m,n} + \beta} \exp(2iK_{m,n}kL_x) \tag{28}$$

Equation (28) specifies the mode reflection coefficient in terms of the normalized termination admittance β, the mode propagation constant $K_{m,n}$, and the nondimensional frequency parameter kL_x.

Source Specification

The final constant to be determined is the modal coupling coefficient $G_{m,n}$, which includes the effects of the source geometry and velocity distribution. In the present study, the source velocity distribution chosen was a rectangular, simply supported plate vibrating in its fundamental mode. Results were obtained for symmetric primary and secondary source locations about the centerline of the y-z plane. (See fig. 1(b).) The source configuration velocity distribution is specified by

$$U(\eta, \varsigma) = U_0[\Phi_p(\eta, \varsigma) + \Gamma \exp(i\phi)\Phi_s(\eta, \varsigma)] \tag{29}$$

where $\Gamma \exp(i\phi)$ specifies the relative amplitude and phase between primary and secondary source velocities. The primary source velocity distribution is given by

$$\Phi_p = \sin\left[\frac{\pi}{\kappa}\left(\varsigma - \frac{1}{2} - \alpha\kappa\right)\right] \sin\left[\frac{\pi}{2\nu}\left(\eta - \frac{1}{2} + \nu\right)\right] \tag{30}$$

where $\kappa = a/L_z$ and $\nu = b/L_y$. (See fig. 1(b).) The nondimensional coordinates η and ς vary over the ranges given by

$$\left(\frac{1}{2} - \nu\right) \le \eta \le \left(\frac{1}{2} + \nu\right) \tag{31a}$$

$$\left(\frac{1}{2} + \alpha\kappa\right) \le \varsigma \le \left(\frac{1}{2} + (\alpha+1)\kappa\right) \tag{31b}$$

The secondary source velocity is given by

$$\Phi_s = \sin\left[\frac{\pi}{\kappa}\left(\varsigma - \frac{1}{2}(\alpha+1)\kappa\right)\right] \sin\left[\frac{\pi}{2\nu}\left(\eta - \frac{1}{2} + \nu\right)\right] \tag{32a}$$

where

$$\left(\frac{1}{2} - \nu\right) \le \eta \le \left(\frac{1}{2} + \nu\right)$$

$$\left(\frac{1}{2} - (\alpha+1)\kappa\right) \le \varsigma \le \left(\frac{1}{2} - \alpha\kappa\right) \tag{32b}$$

Note that 2α is the edge-to-edge source separation measured in source widths, and d (fig. 1(b)) is the center-to-center source separation, where d and α are related by

$$d = (2\alpha + 1)a \tag{33}$$

At the source plane ($\xi = 0$), equation (25) becomes

$$U_{m,n} = \frac{K_{m,n}}{\rho c} G_{m,n} \cos(m\pi\eta)\cos(n\pi\varsigma)(1 - R_{m,n}) \tag{34}$$

This equation gives the acoustic axial particle velocity at the source plane for the (m, n) mode. Such modes can be used to represent the source velocity distribution and thereby satisfy the boundary condition imposed at the source plane. A summation over the mode indices m and n to M and N, respectively, yields

$$U(\eta, \varsigma) \simeq \frac{1}{\rho c} \sum_{m=0}^{M} \sum_{n=0}^{N} K_{m,n} G_{m,n} \cos(m\pi\eta) \times \cos(n\pi\varsigma)(1 - R_{m,n}) \tag{35}$$

The $G_{m,n}$ can be extracted by using the eigenfunction orthogonality condition. The result is

$$G_{m,n} = \frac{4\rho c \lambda_{m,n}}{K_{m,n}(1 - R_{m,n}) L_y L_z} \int\int U(\eta, \varsigma) \times \cos(m\pi n)\cos(n\pi\varsigma)\, d\eta\, d\varsigma \tag{36}$$

where $U(\eta, \varsigma)$ is given by equations (29), (30), and (32a), and the appropriate integration limits are given by equations (31) and (32). Also,

$$\lambda_{m,n} = \frac{1}{4} \quad (m = n = 0)$$

$$\lambda_{m,n} = \frac{1}{2} \quad (m \neq 0,\ n = 0,\ \text{or}\ m = 0,\ n \neq 0)$$

and

$$\lambda_{m,n} = 1 \quad (m \neq 0,\ n \neq 0)$$

Power Into Soft Wall

The expressions for the power radiated by the sources need to be developed at this point. However, it is useful to first introduce some notation changes related to the concept of mode cut-on frequency. It is convenient to calculate acoustic quantities of interest, such as power, as a function of frequency. For the (m,n) mode, excluding the (0,0) mode, the propagation constant $K_{m,n}$ is imaginary for sufficiently low-excitation frequencies. (See eq. (18).) For such values of $K_{m,n}$, the (m,n) mode is said to be cut-off. (See ref. 6.) These imaginary values of $K_{m,n}$ are denoted by

$$K_{m,n} = iK_{m,n}^{(i)} = i\sqrt{\left(\frac{m\pi}{kL_y}\right)^2 + \left(\frac{n\pi}{kL_z}\right)^2 - 1} \quad (37)$$

As excitation frequency increases, $K_{m,n}$ passes zero to take on real values. The frequency at which $K_{m,n} = 0$ is called the cut-on frequency for the (m,n) mode. Above this frequency, the mode propagates as a wave-like disturbance; below this frequency, the mode decays exponentially. Real values of $K_{m,n}$ are denoted by

$$K_{m,n} = K_{m,n}^{(r)} = \sqrt{1 - \left(\frac{m\pi}{kL_y}\right)^2 - \left(\frac{n\pi}{kL_z}\right)^2} \quad (38)$$

All expressions for power and spatially averaged mean-square pressure $\langle\overline{p^2}\rangle$ undergo a change in character upon passing through the cut-on frequency for a given mode. Therefore, in the paragraphs that follow, expressions for power and $\langle\overline{p^2}\rangle$ are presented for a given mode in both cut-off and cut-on states.

For a duct terminated by its characteristic impedance (infinitely long or no reflection), the cut-off modes do not carry power. However, if the duct is not so terminated, then the possibility exists for net power to be carried by the cut-off modes, albeit small relative to the cut-on modes. By integrating the intensity $(1/2\ \mathrm{Re}(pu^*))$ over the absorbing wall for the (m,n) mode, the following result is obtained for the power delivered by the sources to the absorbing wall for the (m,n) mode in its cut-off state:

$$W_{m,n} = \frac{L_y L_z}{4\rho c} |G_{m,n}|^2 K_{m,n}^{(i)} |R_{m,n}| \sin \psi_{m,n} \quad (39)$$

where

$$|R_{m,n}| = \sqrt{\frac{\left(K_{m,n}^{(i)} - \beta^{(i)}\right)^2 + \left(\beta^{(r)}\right)^2}{\left(K_{m,n}^{(i)} + \beta^{(i)}\right)^2 + \left(\beta^{(r)}\right)^2}} \times \exp(-2K_{m,n}^{(i)} kL_x) \quad (40)$$

and

$$\psi_{m,n} = \arctan\left(\frac{K_{m,n}^{(i)} - \beta^{(i)}}{-\beta^{(r)}}\right) - \arctan\left(\frac{K_{m,n}^{(i)} + \beta^{(i)}}{\beta^{(r)}}\right) \quad (41)$$

Examination of the above equations reveals that the maximum power carried by a cut-off mode occurs precisely at the cut-off frequency (i.e., $K_{m,n} = 0$). The power well below the cut-off frequency is negligible because of the dominance of the exponential term, especially if the distance between the source plane and termination L_x is significant.

For a cut-on mode the power delivered to the soft wall is given by

$$W_{m,n} = \frac{L_y L_z}{8\rho c} |G_{m,n}|^2 K_{m,n}^{(r)} (1 - |R_{m,n}|^2) \quad (42)$$

where

$$|R_{m,n}| = \sqrt{\frac{\left(K_{m,n}^{(r)} - \beta^{(r)}\right)^2 + \left(\beta^{(i)}\right)^2}{\left(K_{m,n}^{(r)} + \beta^{(r)}\right)^2 + \left(\beta^{(i)}\right)^2}} \quad (43)$$

If $|R_{m,n}|$ approaches unity for a cut-on mode (i.e., perfect reflection), there is no power transmitted no matter how large the coupling coefficient $G_{m,n}$. On the other hand, if there is no reflection ($R_{m,n} = 0$), the duct carries power only in the positive x-direction. Generally, for $0 < R_{m,n} < 1$, there may be significant interaction between the source and reflected waves which can, in turn, affect $G_{m,n}$ via the term $(1 - R_{m,n})$ in the denominator of the expression for $G_{m,n}$. (See eq. (36).) Therefore, increasing the reflection coefficient may increase the net power flow into the enclosure for particular combinations of source configuration, excitation frequency, and absorbing wall admittance.

Although acoustic power is a convenient measure of overall acoustic coupling efficiency of a given source configuration relative to an acoustic environment, it is the acoustic pressure field that gives rise

directly to the sensation of noise by the human ear. On the other hand, the acoustic pressure may vary dramatically with excitation frequency and receiver position in a semireverberant environment at low modal densities. The goal of this study is more a qualitative understanding of source-enclosure interaction than a detailed study of localized noise reduction in such an environment. It is of interest, however, to compare a measure of spatially averaged sound pressure in the enclosure with power developed by the sources for both cut-off and cut-on modes as follows:

$$\langle \overline{p^2} \rangle = \frac{1}{L_x L_y L_z} \int_0^1 \int_0^1 \int_0^1 pp^* \, d\xi \, d\eta \, d\zeta \qquad (44)$$

For the (m, n) mode in its cut-off state, the result is

$$\langle \overline{P^2} \rangle = \frac{1}{4}|G_{m,n}|^2 \frac{1}{-2K_{m,n}^{(i)} kL_x}[\exp(-2K_{m,n}^{(i)} kL_x) - 1] + 2\,\mathrm{Re}(R_{m,n}) + \frac{|R_{m,n}|^2}{2K_{m,n}^{(i)} kL_x}[\exp(2K_{m,n}^{(i)} L_x) - 1] \qquad (45)$$

where $R_{m,n} = |R_{m,n}| \exp(i\psi_{m,n})$ is defined by equations (40) and (41). For the (m, n) mode in its cut-on state, the result is

$$\langle \overline{P^2} \rangle = \frac{1}{4}|G_{m,n}|^2 \left[1 + \frac{2|R_{m,n}| \sin(2K_{m,n} kL_x + \psi_{m,n}) - \sin(\psi_{m,n})}{2K_{m,n}^{(r)} kL_x} + |R_{m,n}|^2 \right] \qquad (46)$$

where $|R_{m,n}|$ is defined by equation (43) and $\psi_{m,n}$ is given by

$$\psi_{m,n} = \arctan\left(\frac{-\beta^{(i)}}{K_{m,n}^{(r)} - \beta^{(r)}}\right) - \arctan\left(\frac{\beta^{(i)}}{K_{m,n}^{(r)} + \beta^{(r)}}\right) \qquad (47)$$

Equation (46) is characterized by a middle term that approximates $\sin(2K_{m,n}kL_x)/(2K_{m,n}kL_x)$, since $\psi_{m,n}$ is typically small. If the (m, n) mode is being driven well above cut-on, the middle term will likely not be a significant contributor.

In summary, expressions have been developed for calculating the spatial average of the mean-square acoustic pressure and the power delivered to an absorbing enclosure for two symmetrically placed, rectangular velocity sources. The results have been presented in a form that emphasizes the dependence on the frequency parameters kL_x, kL_y, and kL_z; a frequency parameter involving the source separation distance kd; the normalized absorbing wall admittance β; and the secondary or primary source velocity relative amplitude and phase $\Gamma \exp(i\phi)$. Representative results are presented in the following section.

Results and Discussion

It is convenient to use total power reduction as a measure of noise reduction in the semireverberant enclosure; however, the expression for spatially averaged mean-square pressure contained a term which precludes perfect correlation with the expression for power. Therefore, an effort was made to establish the degree to which correlation exists between reductions of power and spatially averaged mean-square pressure. This relation was studied at both the low and high ends of the frequency range. A positive correlation between power and spatially averaged mean-square pressure in a semireverberant enclosure cannot hold in the limit of a fully reverberant enclosure, because there would be no power radiated by the sources, but mean-square pressure would certainly not be zero.

Explicit comparisons of power and spatially averaged mean-square pressure were calculated for enclosure dimensions of $(L_x, L_y, L_z) = (10, 9, 8)$ m, source dimensions of $(a, 2b) = (0.3, 0.6)$ m, and an absorbing wall admittance of $0.1\rho c$. The plots in figures (2) and (3) show comparisons between power and spatially averaged mean-square pressure for 10-Hz bandwidths centered at 45 and 205 Hz, respectively. The modal densities for these two frequencies are approximately 0.8 and 11 modes per hertz, respectively. (See table I.) The top three curves of each figure labeled "0°", "ref," and "180°" show the spatially averaged mean-square pressure $\langle \overline{p^2} \rangle$ for three different source configurations consisting of the primary and secondary sources driven in phase, the primary source alone, and the primary and secondary sources driven 180° out of phase. Note that $\langle \overline{p^2} \rangle$ is expressed in decibels referenced to the calculated value of $\langle \overline{p^2} \rangle$ for the primary source alone driven at the initial frequency. The bottom three curves of each figure likewise show the power level developed by the same source configurations expressed in decibels referenced to 1 watt.

The shaded areas in each figure show what might be achieved in terms of reduction in spatially averaged mean-square pressure or power reduction for a secondary source 180° out of phase with the primary source. Also, "turning on" the secondary source at zero phase causes both $\langle \overline{p^2} \rangle$ and the power to in-

crease by about 6 dB for the low-frequency (short-wavelength) case, which would be expected for a doubling in area of a compact source. At higher frequencies (shorter wavelengths) the configuration exhibits characteristics of extended sources. The main purpose for these two figures, however, is to compare the spatially averaged mean-square pressure inside the enclosure with the power developed by the sources.

A comparison of the power reduction and $\langle \overline{p^2} \rangle$ reduction can be ascertained by comparing the shaded areas between the reference and 180° curves of each figure. Clearly, there is excellent qualitative agreement for the 10-Hz bandwidth centered at 45 Hz. For the 10-Hz bandwidth centered at 210 Hz, the correlation is good, but there are some differences in the neighborhood of the sharp peaks. It will be shown in subsequent figures that the sharper peaks are associated with cut-on frequencies of the "duct-like" modes of the enclosure. Also, a dramatic degradation in the noise reduction is apparent in figure 3 compared with that of figure 2. This degradation is discussed in more detail subsequently. The focus of interest presently is that reductions in power output correlate well with reductions in $\langle \overline{p^2} \rangle$ at both the low and high end of the frequency range. As discussed in the section "Analysis," the term involving $\sin(2K_{m,n}kL_x)/(2K^{(r)}_{m,n}kL_x)$ in equation (46) is a potential contributor to $\langle \overline{p^2} \rangle$ near mode cut-on frequencies. However, for the modal power, this term is absent, which may account for the localized differences between $\langle \overline{p^2} \rangle$ reduction and power reduction at the higher frequencies. To recapitulate, it appears that reductions in spatially averaged mean-square sound pressure level correlate well with reductions in sound power level for modal densities from about 0.8 to 11 modes per hertz in a semireverberant rectangular enclosure. Therefore, the effects of source separation, size, phasing, and wall admittance obtained by studying only the changes in the sound power levels are discussed in the sections that follow.

Effect of Secondary Source Phase and Source Separation

The effects of incremental phase changes of the secondary source on the combined power developed by several primary and secondary source configurations are examined in this section. Figures 4(a) to 4(d) show the effects of secondary source phase increments of 30° on the combined power output of the primary and secondary source configuration. Each plot shows power level in dB referenced to 1 W versus frequency for secondary source phase parameter ranging from 0° to 180° for a given source separation. At the top of each figure is shown the range of the separation parameter kd for the particular source separation shown in the sketch on the right-hand side of the figure. The figure includes the soft-wall admittance value and the plot symbols for the phase parameter. The frequencies of the power response maxima correlate with the hardwall enclosure modal resonant frequencies, as listed in table II, that were calculated from equation (20). Included in the figures are the hardwall enclosure mode order designations associated with these maxima.

In particular, figure 4(a) shows the effect of secondary source phasing on total output power when the source center-to-center separation is set to the minimum of one source width for the smallest source width used in this study. (See table I.) For phase differences ranging from 0° through 150°, the power output is dominated by three maxima. These maxima are labeled by modal indices corresponding to the hardwall enclosure modal resonant frequencies of 41.85, 42.94, and 46.25 Hz (see table II). As shown in figure 4(a), these frequencies correspond closely to the frequencies at which the maximum power responses of the semireverberant enclosure occur. For a secondary phase difference of 180°, however, the character of the power response curve changes dramatically, because the even-mode component associated with the z-axis direction cannot be driven with an asymmetric source velocity distribution. The correspondence between rigid enclosure modal resonances and the soft-wall enclosure modal behavior is expected, because the admittance is chosen small to make the enclosure highly reverberant. Also, the "break-even" phase angle (defined in discussion of fig. 5) at which the combined output power of the primary and secondary source configurations is very nearly equal to the primary source power alone is about 120°. This phase angle arises from the effects of the interaction of two compact sources in close proximity, and appears mathematically as $2U_0\Phi_p\Phi_s\cos\phi$ when the quantity UU^* is calculated using equation (29). This quantity enters the power calculation through the factor $|G_{m,n}|^2$ in equation (39). When the secondary and primary phase differences are 180°, the minimum and maximum power reductions across the entire 10-Hz bandwidth are about 12 and 34 dB, respectively. This substantial noise reduction is consistent with the small source separation relative to the wavelength ($0.22 < kd < 0.27$) and the source compactness ($0.22 < ka < 0.27$).

Figure 4(b) shows the power developed by the sources at secondary source phase increments of 30° for a source separation of 9 source widths. The key feature of this result compared with that of figure 4(a) is the absence of a relatively uniform reduc-

tion in power as the phase increases toward 150°. There is a substantial decrease in power between 41 and 43 Hz. In the frequency range 43.4 to 49 Hz, the power generally increases with increasing phase difference. As shown in figure 4(a) these changes in the power with changing phase again correlate with the excitation of particular modes that can be identified with hardwall enclosure modes. The (1,2,0) and (0,0,2) modes are symmetrical in the $y-$ and $z-$directions and are therefore annihilated when the phase difference attains a value of 180°. On the other hand, the (0,2,1) and (1,2,1) modes are asymmetrical in the z-direction and are accentuated as the phase increases toward 180°.

The source separation in figure 4(c) has been increased to 17 source widths. The power reduction achieved for this separation is less than that for the case with a separation of 9 source widths and is likewise associated only with the annihilation of the (1,2,0) mode as the phase increases toward 180°. Again, as in figure 4(b), there is significant power increase over the frequency range 43 to 50 Hz with increasing phase. Clearly, the (0,2,1) and (1,2,1) modes couple to this source separation better than for the 9-source-width separation shown in figure 4(b).

For the limiting source separation of 25.6 source widths (fig. 4(d)), the general trend is similar to those of figures 4(b) and (c). There is slight degradation in power reduction from 41 to 43 Hz, and the (1,0,2) mode is driven more strongly for this separation. Figures 4(a) to (d) summarize the detailed effects on total power output of dephasing the secondary source with respect to the primary source in steps of 30° from 0° to 180°. In general, increasing source separation causes the enclosure mode response to change dramatically, which in most cases results in degradation of achievable power reduction. Figures 5(a) to (d) use the 0° and 180° plots from figures 4(a) to (d) to emphasize the output power reduction achievable relative to the power output of the primary source alone when the secondary source is driven 180° relative to the primary source.

Sound Power Reductions for Secondary Phase of 0° and 180°

Figures 5(a) to (d) show output power versus frequency for the same four source separations discussed previously, but each source configuration is operating in three different states, corresponding to the three curves shown in the figures. The top curve, denoted by the circles, corresponds to both sources operating in phase; the curve denoted by the diamonds represents the power level for the primary source alone; finally, the curve denoted by the squares represents the output power level for both sources operating 180° out of phase. For both primary and secondary sources "turned on," the velocity amplitudes are equal, as indicated by the velocity ratio parameter Γ in the figure key. The curve representing the power output for the primary source alone is taken as a reference or break-even power level, which the combined primary and secondary output must equal to obtain a payoff from an active control viewpoint. The shaded areas between the curves represent the potential sound power reduction over the 10-Hz bandwidth for the particular source separation shown in the sketch, on the right-hand side of each figure for both 0° and 180° relative phase. A different type of shading corresponds to reductions achieved for each of the two control source phasings considered.

Figure 5(a) shows that net power reductions ranging from 10 to 25 dB can be achieved over the entire 10-Hz bandwidth for the minimum separation of 1 source width. In figure 5(b), the source separation is 9 source widths. Clearly, a marked degradation in the potential for sound power reduction occurs with this increased source separation. However, over a 1-Hz interval centered at 42 Hz, a reduction of up to 8 dB is still achievable. Up to 3-dB reductions also appear in the vicinity of 44 and 47 Hz. In figure 5(c), the separation is 17 source widths. For this separation, the frequency interval and magnitude of power reduction centered at 42 Hz decreased; however, the regions of reduction associated with the two higher frequencies of 44 and 47 Hz increased and coalesced into a single continuous region to yield power reduction ranging up to 8 dB. Finally, for the maximum separation of 25.6 source widths (fig. 5(d)), the frequency intervals of power reduction become more limited with maximum reductions of about 5 dB. Figures 5(a) to (d) demonstrate that small source separation gives consistent reductions across at least 10-Hz bandwidths, whereas large source separation gives no systematic result across the same 10-Hz bandwidth. However, at frequencies where reductions do occur at large separations, the reductions may still be significant. Generally, as source separation increases, the magnitudes and bandwidths of the sound power reductions appear to decrease.

Source Size Effects

Effects of source size on power reduction were examined. Power level reductions for minimum and maximum source separations are presented for a 10-Hz bandwidth centered at 45 Hz and a 10-Hz bandwidth centered at 205 Hz.

Figures 6(a) to (c) show the effects of source size on power reduction for the secondary source driven

at a phase of 0° or 180°. The source separation parameter kd ranged from 1.98 to 2.47 for all three source sizes. Comparison of the shaded areas for figures 6(a) to (c) shows great similarity in the noise reductions as the source size changes, although there is some degradation in power reduction for the largest source size shown in figure 6(c). These results suggest that for values of kd between 2.0 and 2.5, power level reduction scales with kd, but is invariant with source size parameter ka up to a value of 2.5.

Figures 7(a) to (c) show the effects of source size on power reduction for the secondary source driven at a phase of 0° or 180° over the frequency range of 200 to 210 Hz or over the kd range from 9.87 to 10.37 and over the ka range from 1.10 to 10.22. No consistent reductions are observed in this frequency range for the three different source sizes. In fact, no significant power reduction is present except for the minimum source separation (limited by edge contact) of figure 7(c). For the source separation of figure 7(c), both the separation parameter kd and the source compactness parameter ka range from 9.87 to 10.37. It appears that a modest power reduction can be obtained even for noncompact sources if the separation distance is minimized. However, for the larger sources the power reduction does not scale with kd.

Effect of Enclosure Size

Figures 8(a) to (c) illustrate the effect of enclosure size on power reduction. For successive doublings of the enclosure dimensions, the ranges of the source size parameter ka and source separation parameter kd are held constant although the enclosure size parameter kL_x assumes a different range for each figure. The kL_x ranges are depicted at the bottom of each plot. The minimum value of kL_x is 7.3, and the maximum value is 33.0. As in the preceding figures, sketches of source placement relative to the bounding enclosure walls are included. For the source size chosen, the maximum separation of 5 source widths is determined by the smallest enclosure size. (See fig. 8(a).)

Comparison of the power reductions for enclosures differing in size by a factor of four indicates no consistent trends over a source separation parameter kd range of 1.1 centered on a value of approximately 5.0. However, at those frequencies at which power decreases do occur, they range as high as 8 dB.

Effect of Impedance Changes

The remaining figures deal with effects of changing the absorbing wall admittance. All the previous results were based on a normalized admittance of 0.1, which corresponds to a relatively hard wall. Comparative results are presented for normalized admittance β values of 0.1, $0.1 + 0.1i$, and 0.2 for the intermediate source size (see table I) at the minimum and maximum source separation distances.

Figures 9(a) to (c) show the effect of increasing the normalized soft-wall admittance through the respective values 0.1, $0.1 + 0.1i$, and 0.2 at the minimum source separation. Results are presented over the frequency range from 40 to 50 Hz. For the admittance increment of 0.1 in the imaginary component, there are observable but relatively minor changes in the shapes of the power reduction regions. (See fig. 9(b).) For the admittance increment of 0.1 in the real component (fig. 9(c)), there are significant changes in the shapes of the power reduction regions, but a general similarity in behavior to figures 9(a) and (b) is evident. Figures 10(a) to (c) show the results for a similar computation for the maximum source separation of 5 source widths.

Again, there are relatively minor changes in the regions of power reduction for the increment in the imaginary component. An increment of 0.1 in the real component, however, causes a substantial decrease in the power reduction. Thus, for this frequency range, a change of 0.1 in the real component of β appears to have consistently greater effect than the same change in the imaginary component of β.

The remaining figures (11(a) to (c) and 12(a) to (c)) show the same sequence of parametric plots depicting effects of incremental changes in soft-wall admittance for the high end of the frequency range (a 10-Hz bandwidth centered on 205 Hz). For this frequency range, there is little change in the power reductions for a separation of 1 source width as the imaginary admittance component increases by 0.1. (See figs. 11(a) and (b).) In figures 12(a) and (b), for the maximum source separation, there is again little change for the increment in the imaginary admittance component. In contrast, figure 12(c) shows that for the increment in the real component, there is no observable power reduction achieved due to the secondary source for either choice of phase. The results shown in figures 12(a) to (c) for the high frequency range thus exhibit trends similar to those seen in figures 11(a) to (c) for the low frequency range.

Concluding Remarks

Acoustic power radiated by two mutually interacting, rectangular velocity sources into a semireverberant enclosure was studied to determine the relative significance of controlling parameters as applied to active noise control. The ranges of parameter values were sufficient to conclude that the power re-

duction is very sensitive to source size, separation, and phase. In general, the results obtained suggest that for low modal densities in a semireverberant enclosure, significant noise reductions are achievable for compact sources. However, for larger sources at higher modal densities, only modest power reductions can be obtained, and these reductions degrade as the primary-to-secondary source separation parameter increases.

Source location symmetry considerations indicate that reduction in net radiated power to the enclosure is caused by changes in the radiation impedance on each source surface. These changes in mutual radiation impedance are directly related to changes in the acoustic pressure field in the enclosure and are strongly dependent on source separation and phase. Reflections from the absorbing wall also affect the source radiation load; however, under semireverberant conditions, minor changes in absorbing wall admittance are of secondary importance.

These results suggest that active control of discrete frequency noise in a semireverberant enclosure depends on many interacting parameters. Power radiated by a primary or secondary source configuration varies markedly with changes in some parameters over critical ranges. Estimates of noise reduction achievable for aircraft cabin interiors requires calculations for more realistic enclosure geometries and acoustic absorption characteristics. Also, source configurations involving the interaction of multiple primary and control sources on opposite walls should be considered as a model for the acoustic transmission through aircraft fuselage sidewalls.

NASA Langley Research Center
Hampton, VA 23665-5225
June 19, 1985

References

1. Warnaka, Glenn E.: Active Attenuation of Noise- The State of the Art. *Noise Contr. Eng.*, vol. 18, no. 3, May June 1982, pp. 100-110.
2. Leventhall, H. G.: Active Attenuators: Historical Review and Some Recent Developments. *Noise Control for the 80's- Proceedings Inter-Noise 80, Volume II.* George C. Maling, Jr., ed., Noise Control Foundation, 1980, pp 679 682.
3. Conover, William B.: Fighting Noise With Noise. *Noise Contr.*, vol. 2, no. 2, Mar. 1956, pp. 78 82.
4. Ross, C. F.: Experiments on Active Control of Transformer Noise. *J. Sound & Vib.*, vol. 61, no. 4, Dec. 22, 1978, pp. 473 480.
5. Zalas, J. M.; and Tichy, J.: *Active Attenuation of Propeller Blade Passage Noise.* NASA CR-172386, 1984.
6. Morse, Philip M.: and Ingard, K. Uno: *Theoretical Acoustics.* McGraw-Hill Book Co., Inc., c.1968.
7. Richards, E. J.; and Mead, D. J., eds.: *Noise and Acoustic Fatigue in Aeronautics.* John Wiley & Sons, Ltd., 1968.

TABLE I. PARAMETER RANGES FOR FIGURES 4 THROUGH 12

Parameter	Figures 4 and 5	Figure 6	Figure 7	Figure 8	Figures 9–12
Enclosure dimensions:					
L_x, m	10	10	10	2.5, 5.0, 10	10
L_y, m	9	9	9	2.3, 4.5, 9	9
L_z, m	8	8	8	2.0, 4.0, 8	8
Source dimensions:					
a, m	0.3	0.3, 1.3, 2.7	0.3, 1.3, 2.7	0.3	1.3
$2b$, m	0.6	0.6, 2.7, 5.3	0.6, 2.7, 5.3	0.6	2.7
Source center separation (source widths)	1, 9, 17, 25.6	9, 2, 1	9, 2, 1	5	1, 5
Absorbing wall admittance (normalized to ρc)	0.1	0.1	0.1	0.1	0.1; 0.1 + 0.1i; 0.2
Frequency, Hz	40–50	40–50	200–210	160–180	40–50; 200–210
Modal density (number of modes/Hz)	0.65–0.92	0.65–0.92	10.3–11.2	0.16–0.20 0.99–1.2 6.8–8.4	0.65–0.92 10.3–11.2
Source separation, kd	0.22–0.27 2.0–2.5 3.7–4.7 5.6–7.0	2.0–2.5	10.0–10.4	4.4–4.9	0.98–1.2 4.9–6.1 24.3–25.5
Source width, ka	0.22–0.27	0.22–0.27 1.0–1.2 2.0–2.4	1.1–1.2 4.9–5.1 9.8–10.2	0.88–0.99	0.98–1.2 4.9–5.1
Enclosure dimension, kL_x	7.3–9.2	7.3–9.2	36.6–38.4	7.3–8.2 14.6–16.5 29.3–32.9	7.3–9.2 36.6–38.4

TABLE II. EIGENMODE FREQUENCIES FOR REVERBERANT ENCLOSURE ARRANGED IN MONOTONIC ORDER

[$L_x = 10$ m; $L_y = 9$ m; $L_z = 8$ m; $c = 343.5$ m/sec]

ℓ, m, n	$f_{\ell,m,n}$
1, 0, 0	17.18
†0, 1, 0	19.08
†0, 0, 1	21.47
1, 1, 0	25.67
1, 0, 1	27.49
†0, 1, 1	28.72
1, 1, 1	33.47
2, 0, 0	34.35
†0, 2, 0	38.17
2, 1, 0	39.29
2, 0, 1	40.51
1, 2, 0	41.85
†0, 0, 2	42.94
†0, 2, 1	43.79
2, 1, 1	44.78
1, 0, 2	46.25
†0, 1, 2	46.99
1, 2, 1	47.04
1, 1, 2	50.03

†Zero-order, x-axis modes.

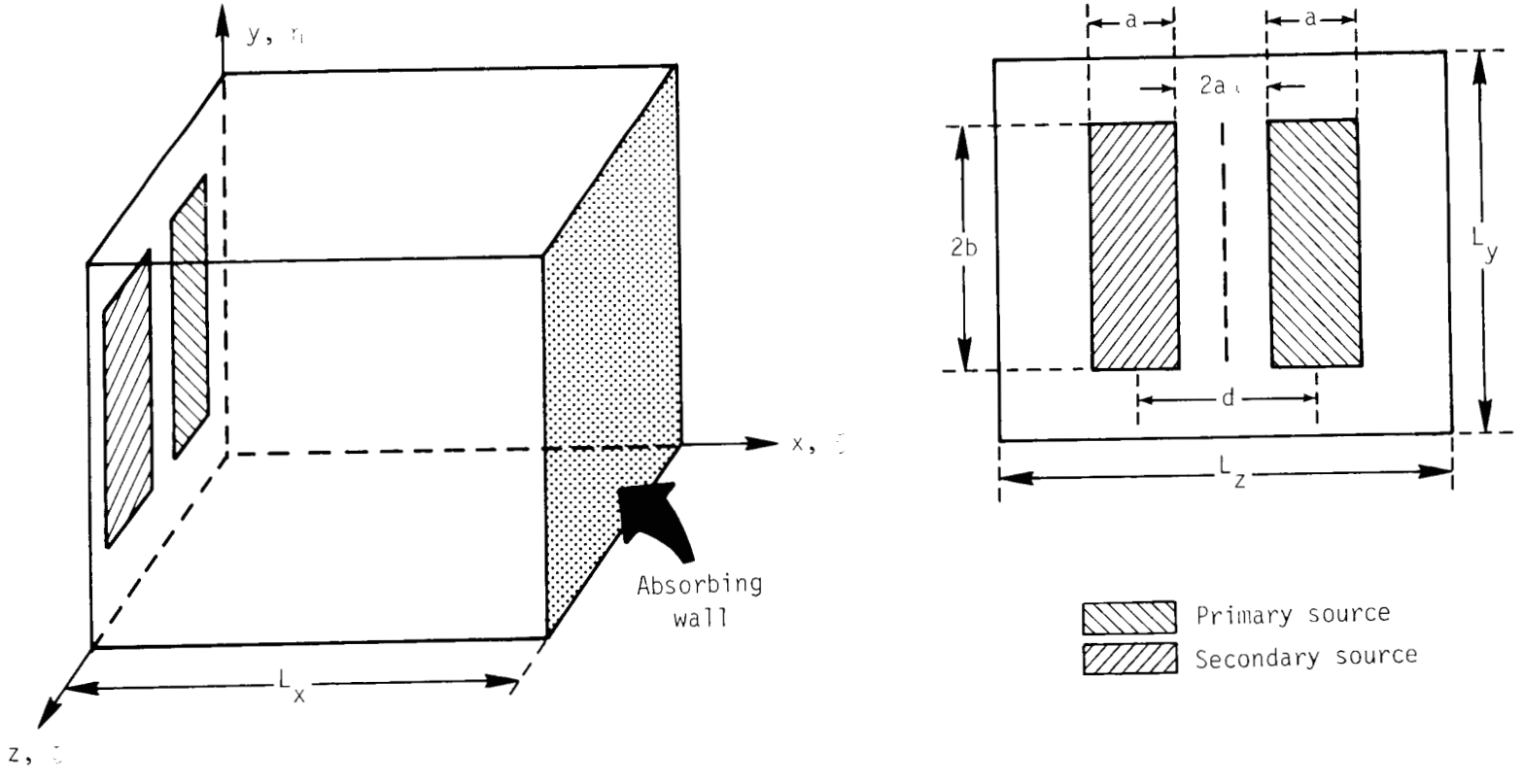

(a) Semireverberant space.

(b) Source wall.

Figure 1. Schematic of semireverberant enclosure and source configuration for parametric study of active noise control concept.

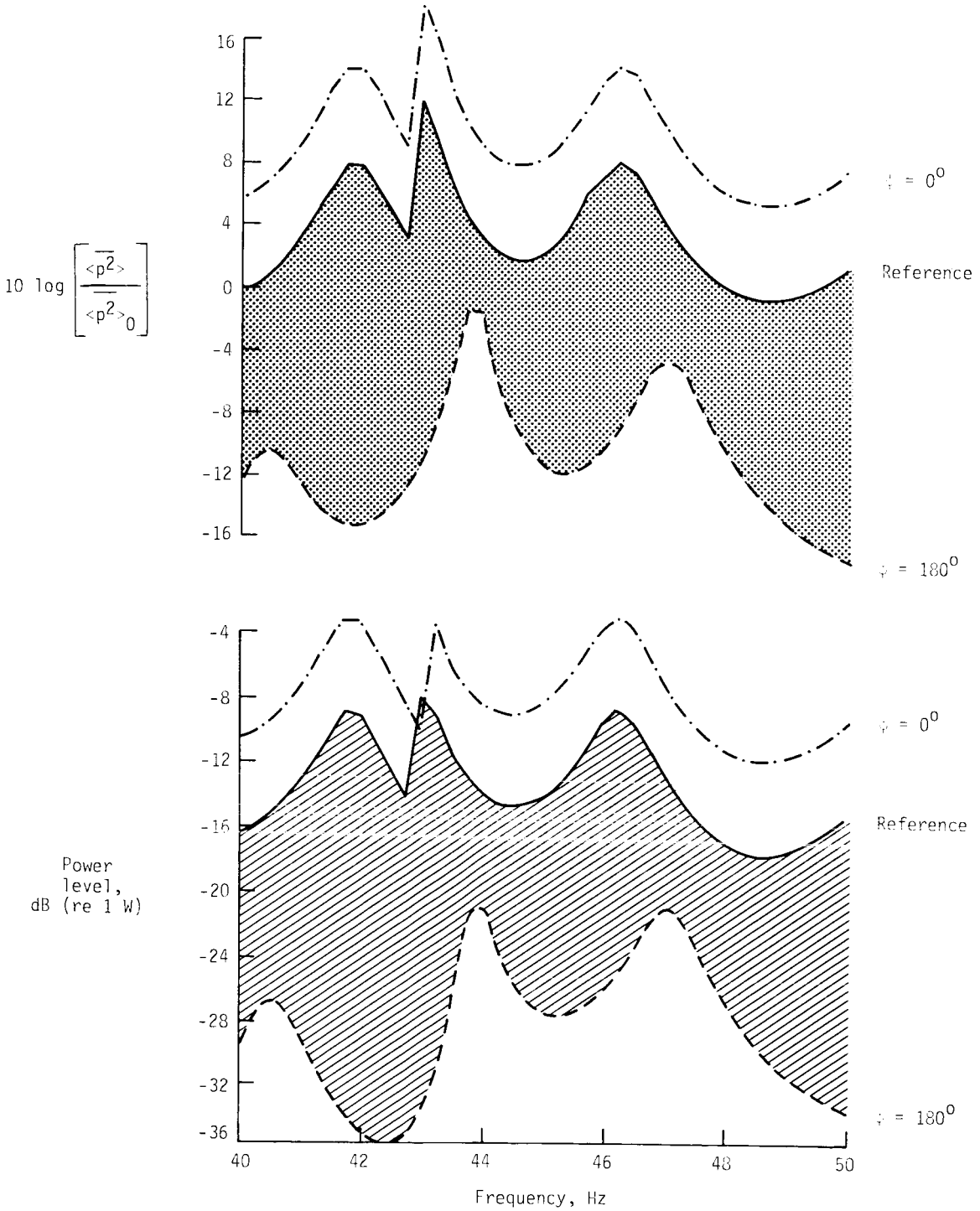

Figure 2. Comparison of power and spatial average of mean-square pressure. 40 50 Hz. $d = 1$ source width.

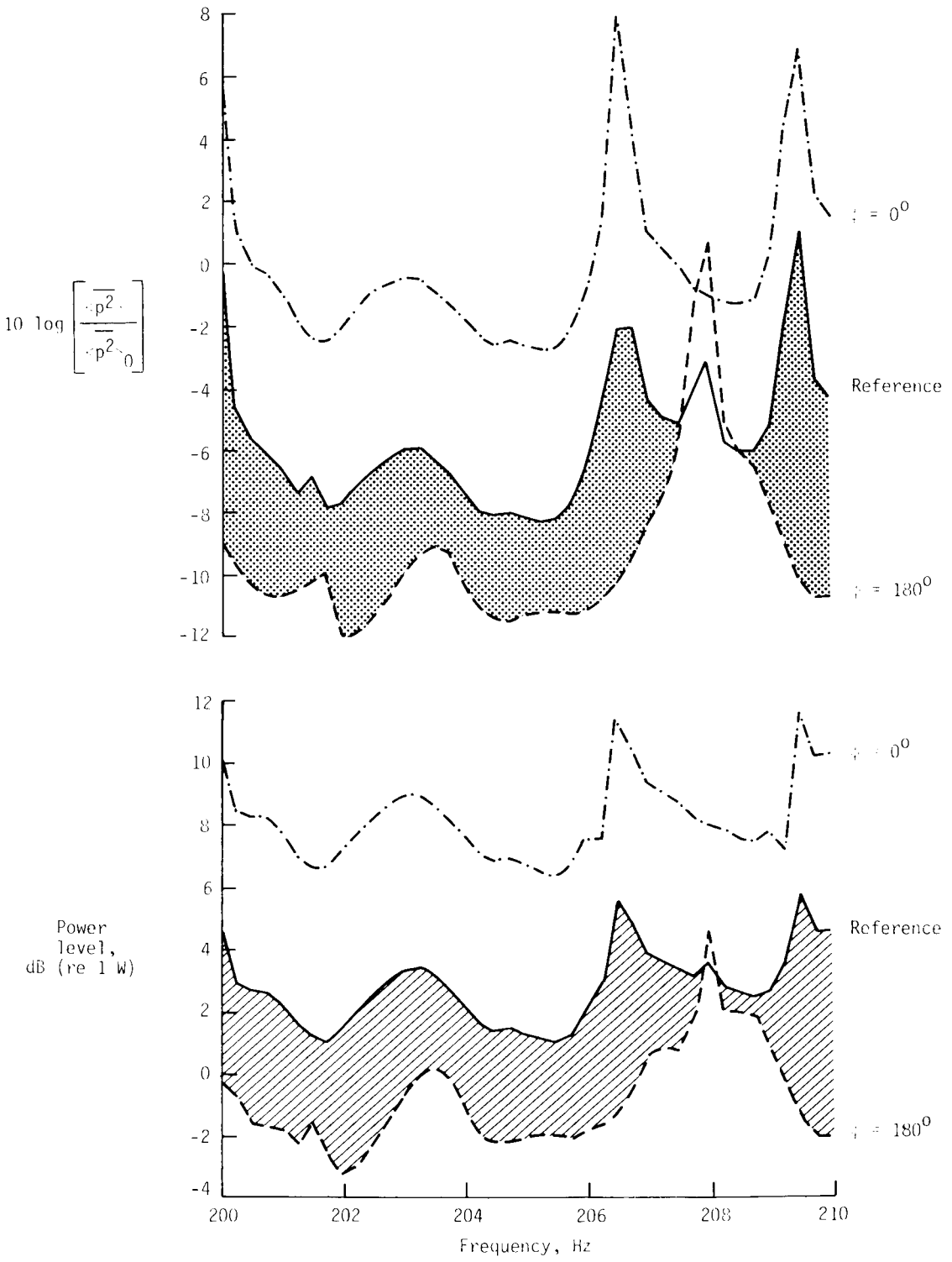

Figure 3. Comparison of power and spatial average of mean-square pressure, 200–210 Hz. d = 1 source width.

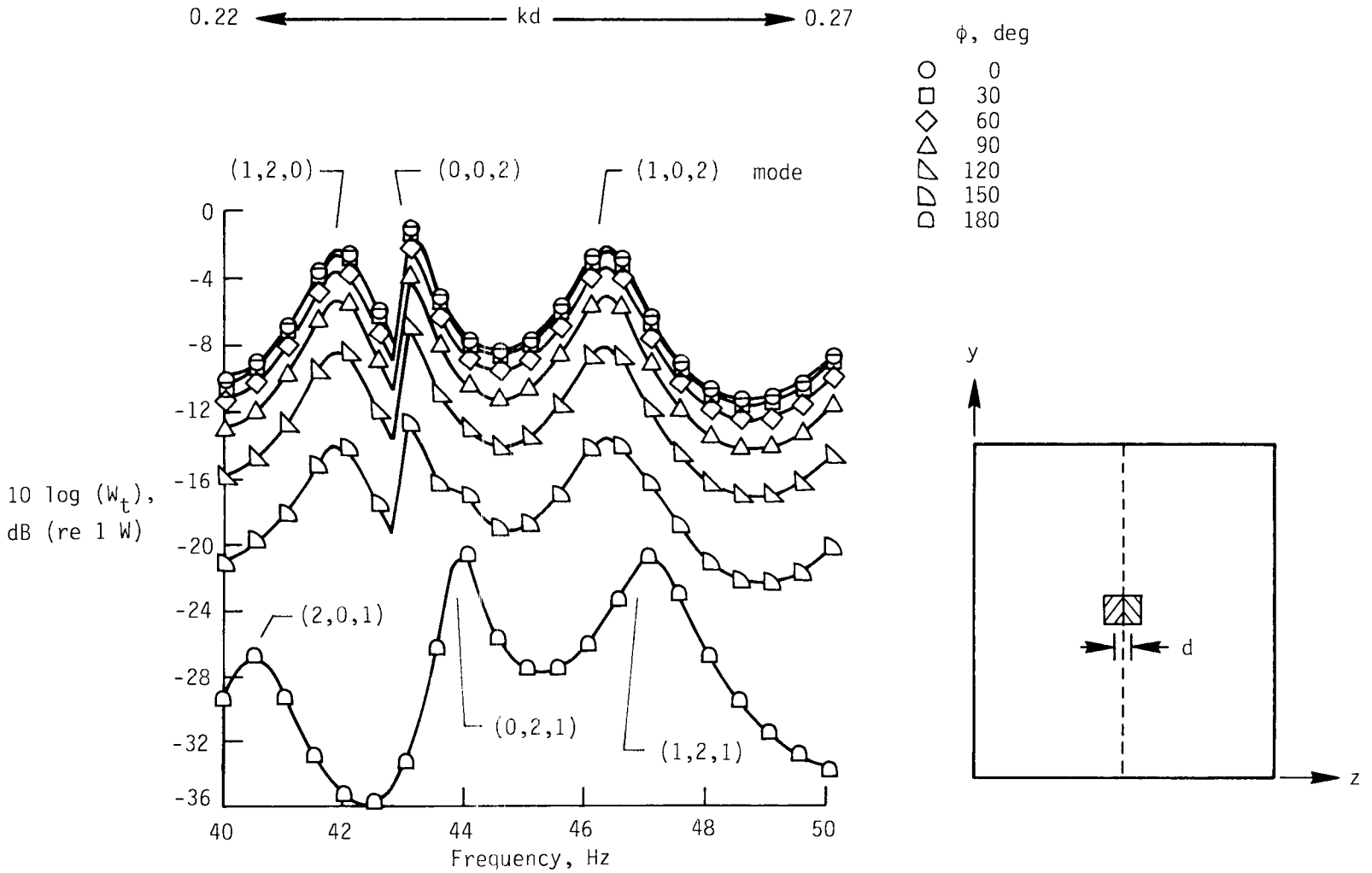

(a) $d = 1$ source width.

Figure 4. Effect of secondary source phase on total power level for three source separations. $\beta = 0.1$.

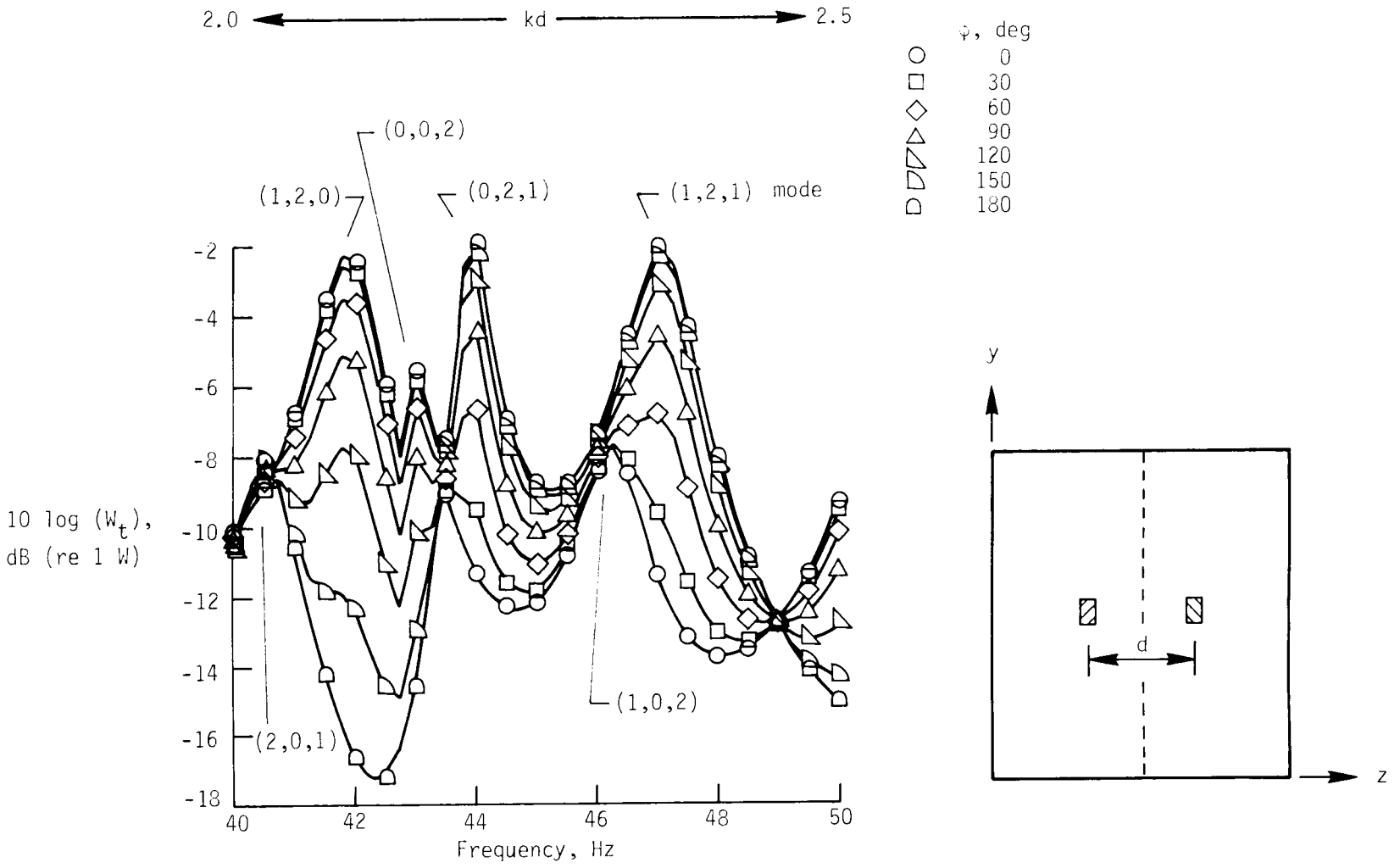

(b) $d = 9$ source widths.

Figure 4. Continued.

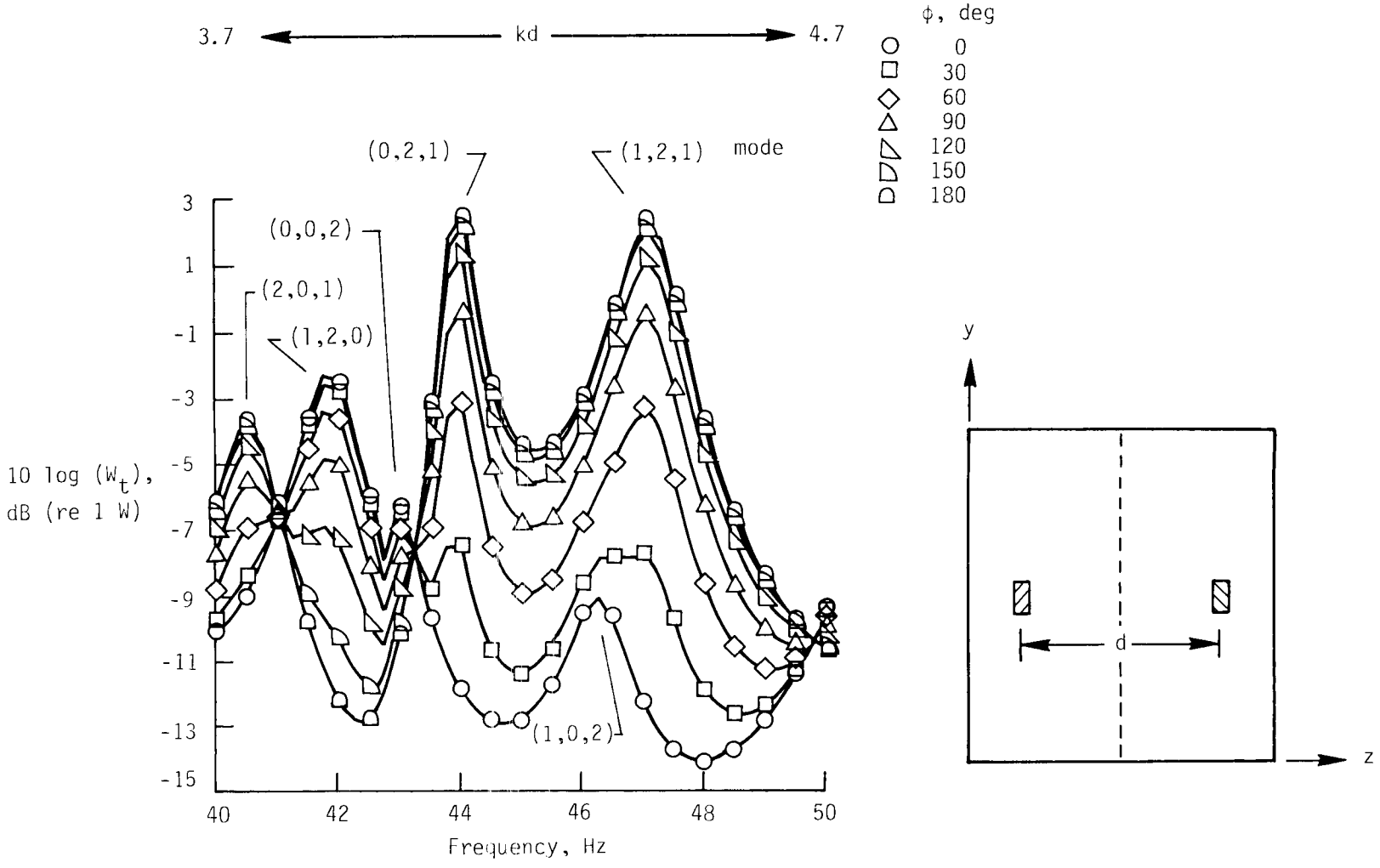

(c) $d = 17$ source widths.

Figure 4. Continued.

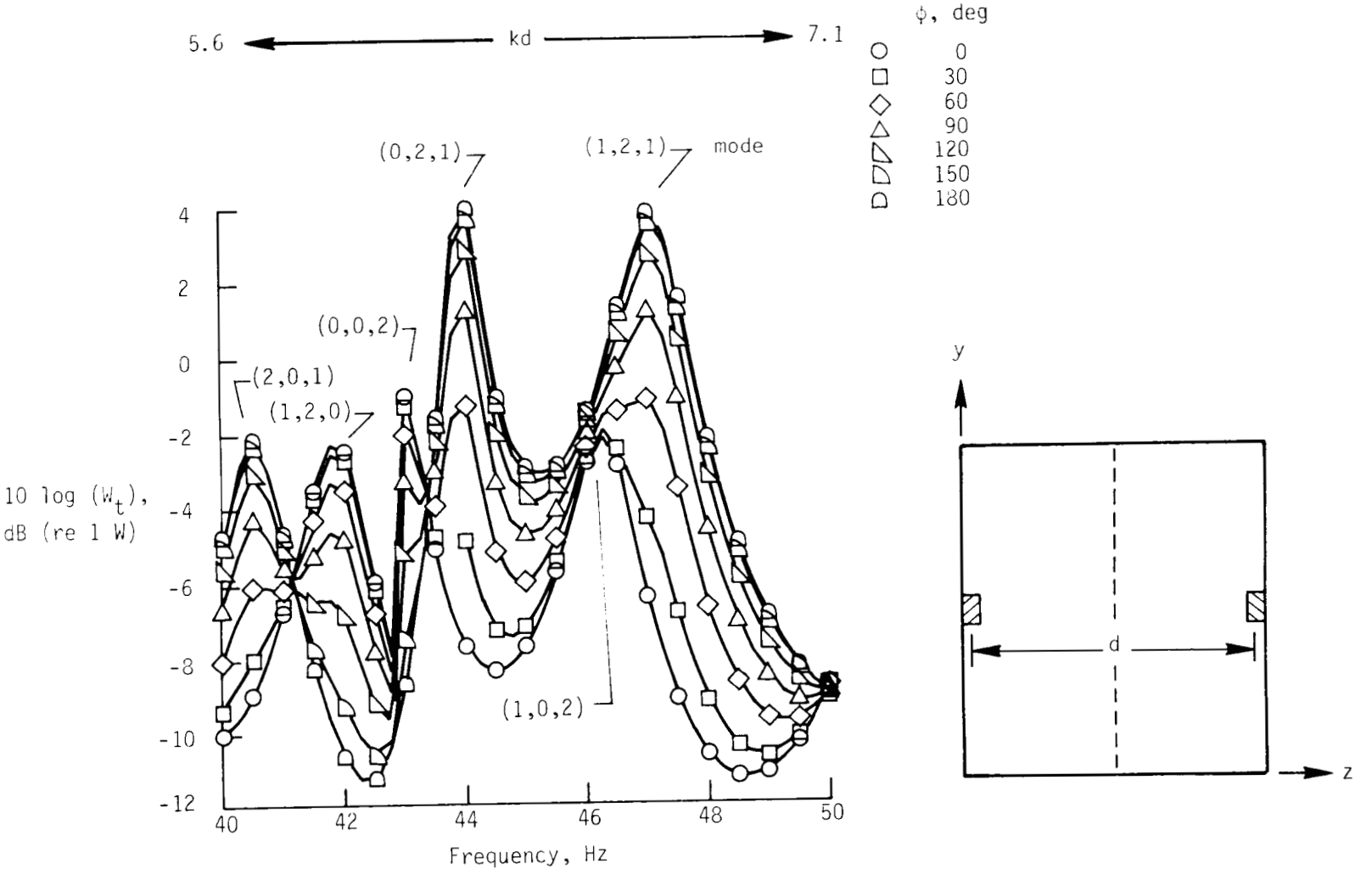

(d) $d = 25.6$ source widths.

Figure 4. Concluded.

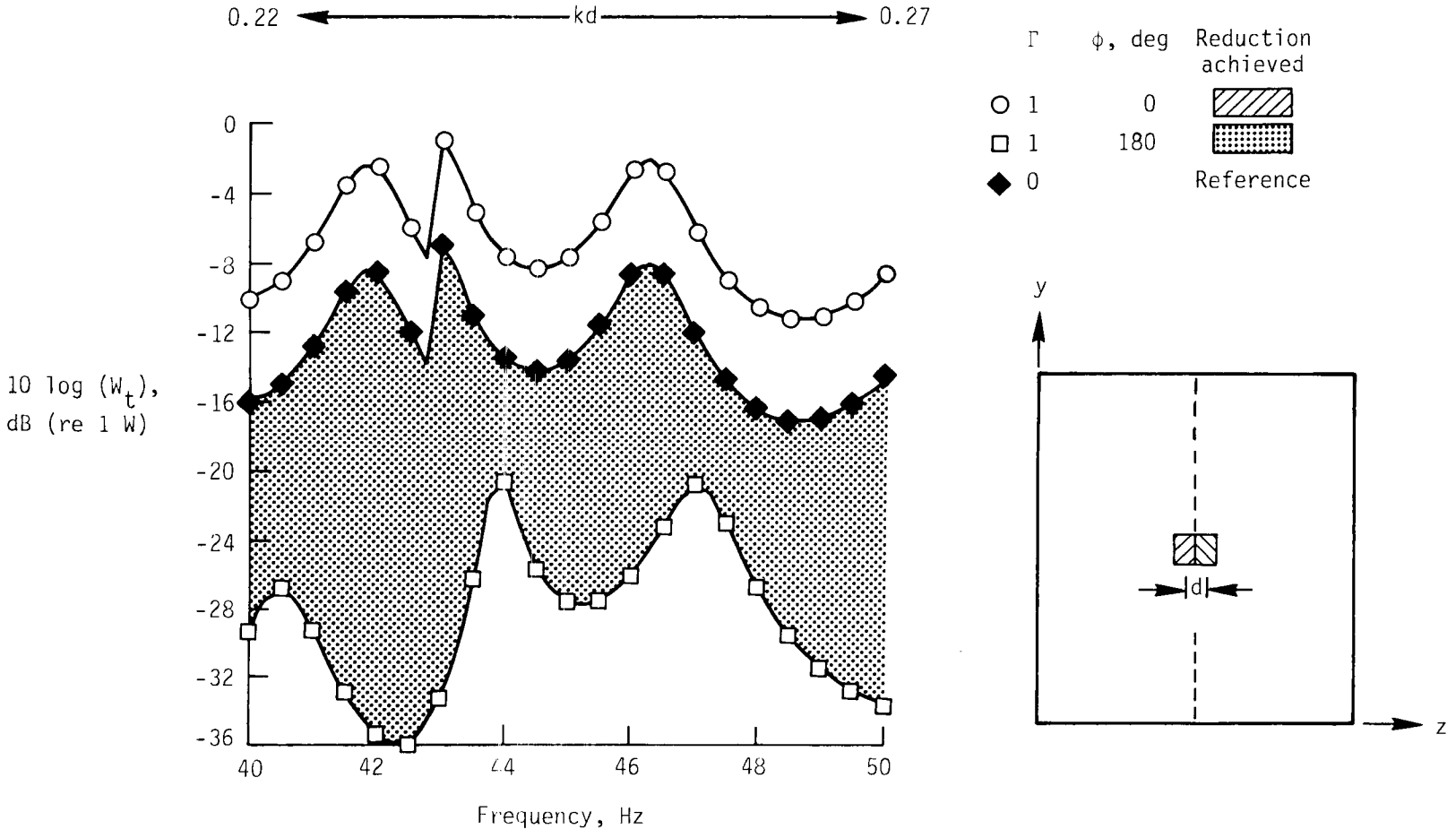

(a) $d = 1$ source width.

Figure 5. Effect of secondary source at 0° and 180° phase on total power level. $\beta = 0.1$.

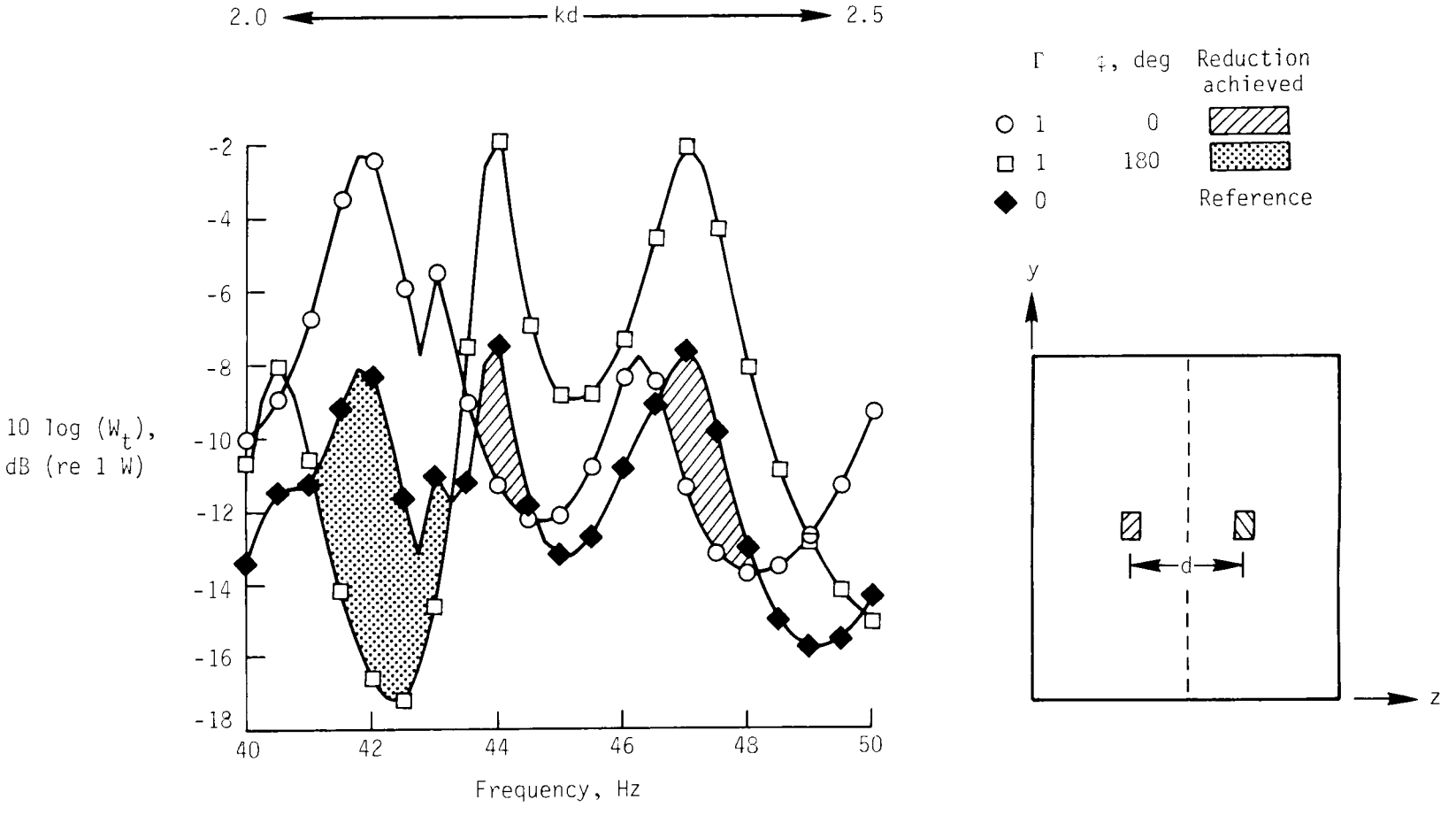

(b) $d = 9$ source widths.

Figure 5. Continued.

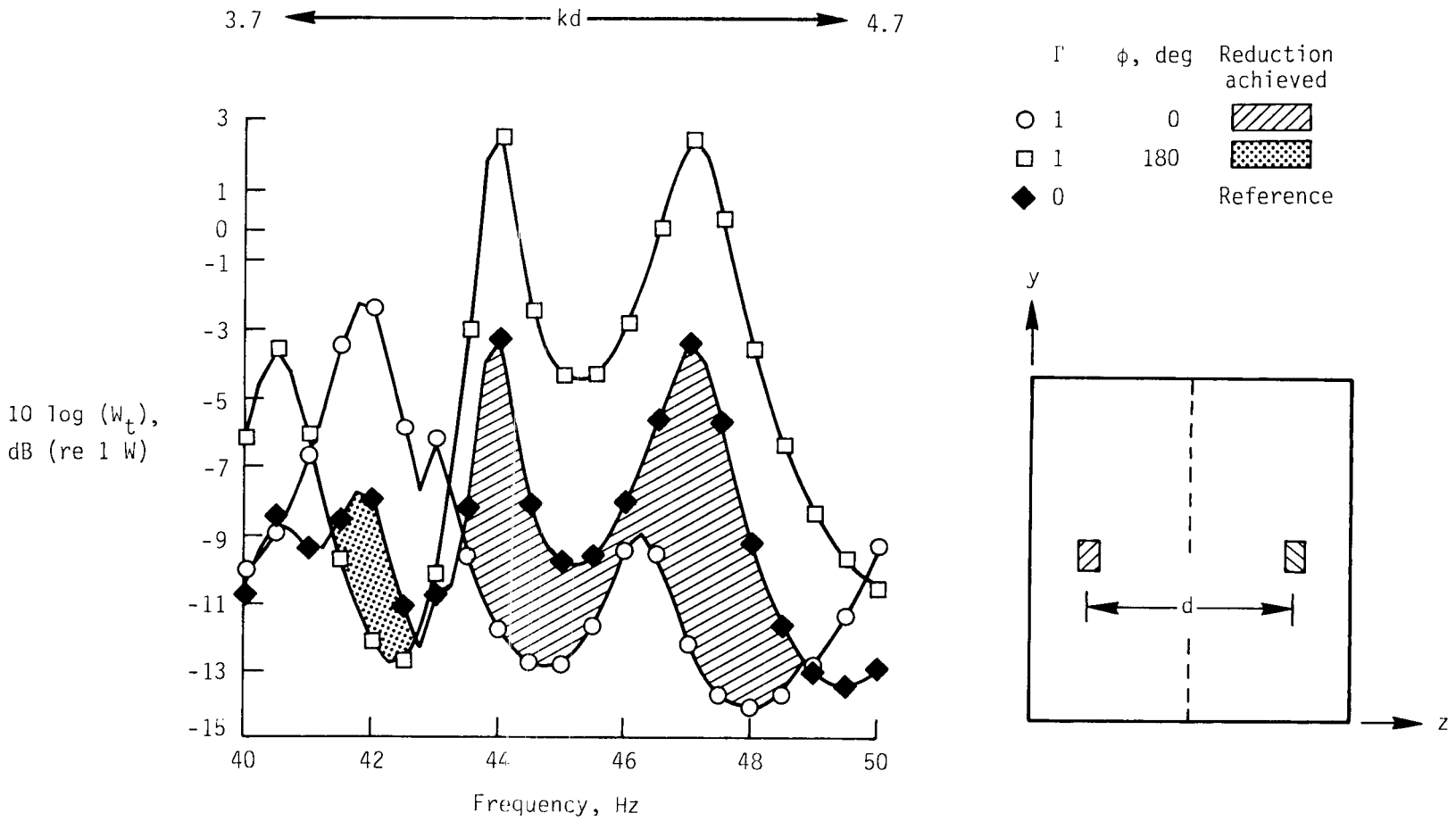

(c) $d = 17$ source widths.

Figure 5. Continued.

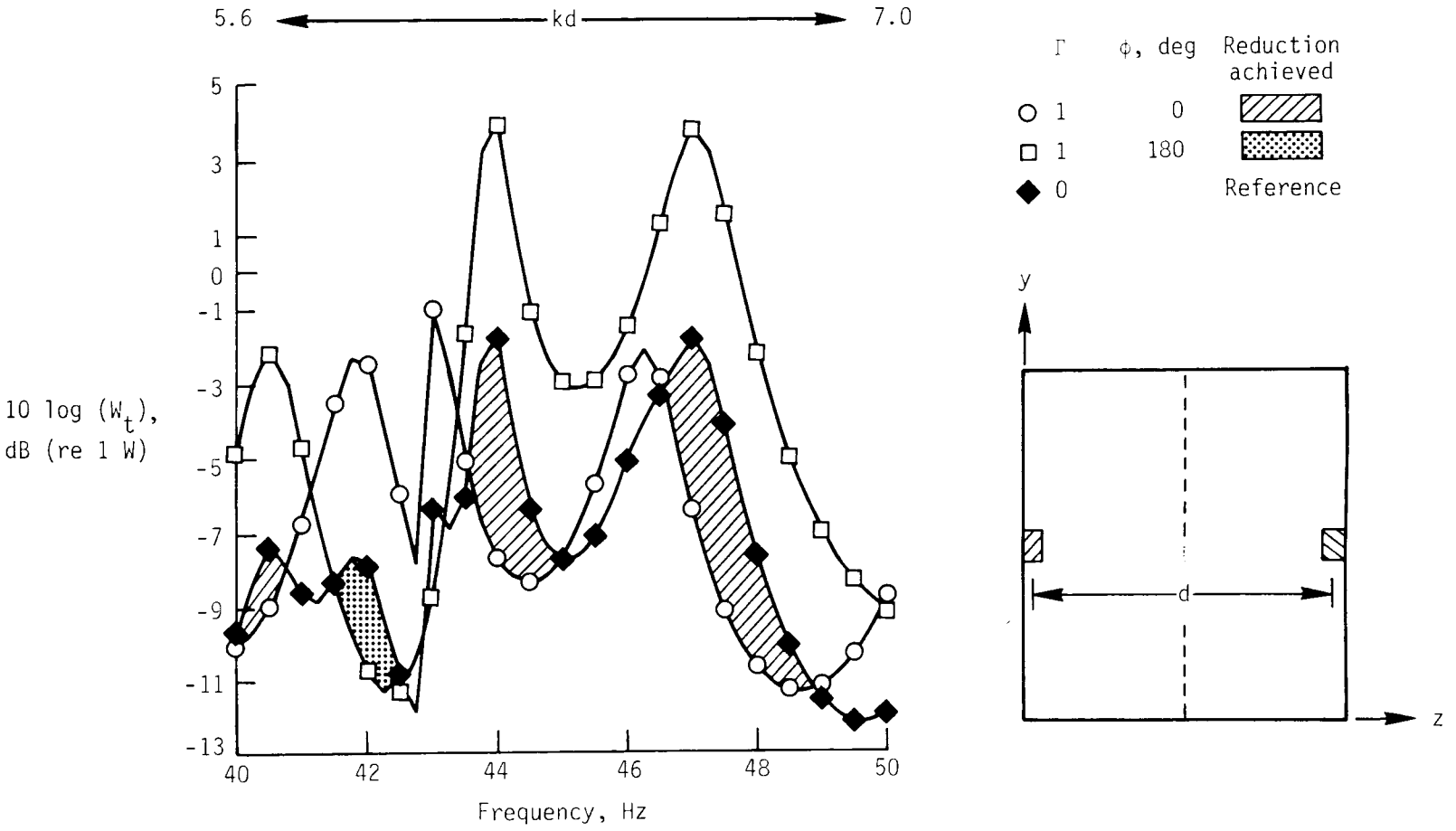

(d) $d = 25.6$ source widths.

Figure 5. Concluded.

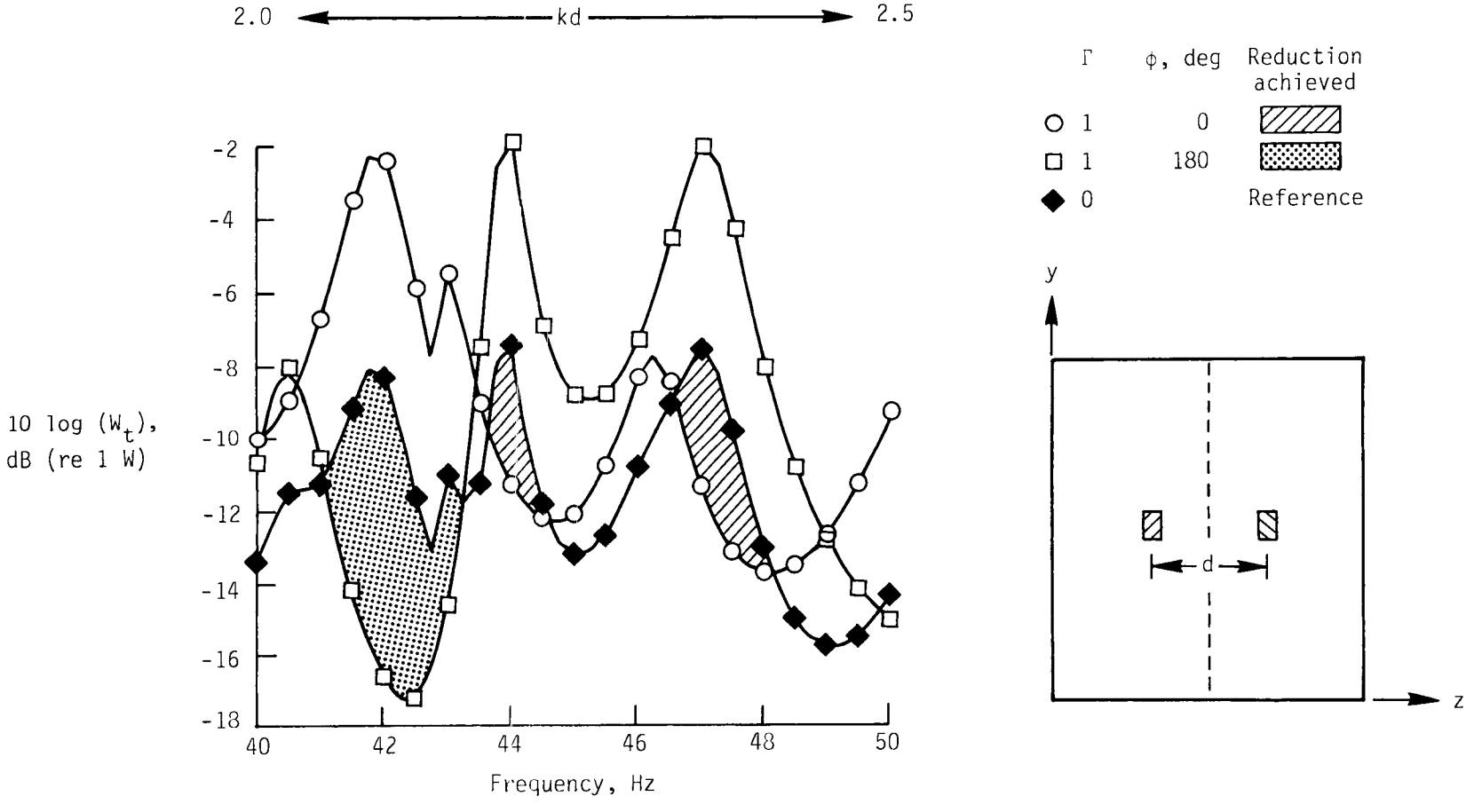

(a) $a = 0.3$ m; $2b = 0.6$ m; $d = 9$ source widths.

Figure 6. Effect of secondary source size on total power level, low frequency case. $\beta = 0.1$.

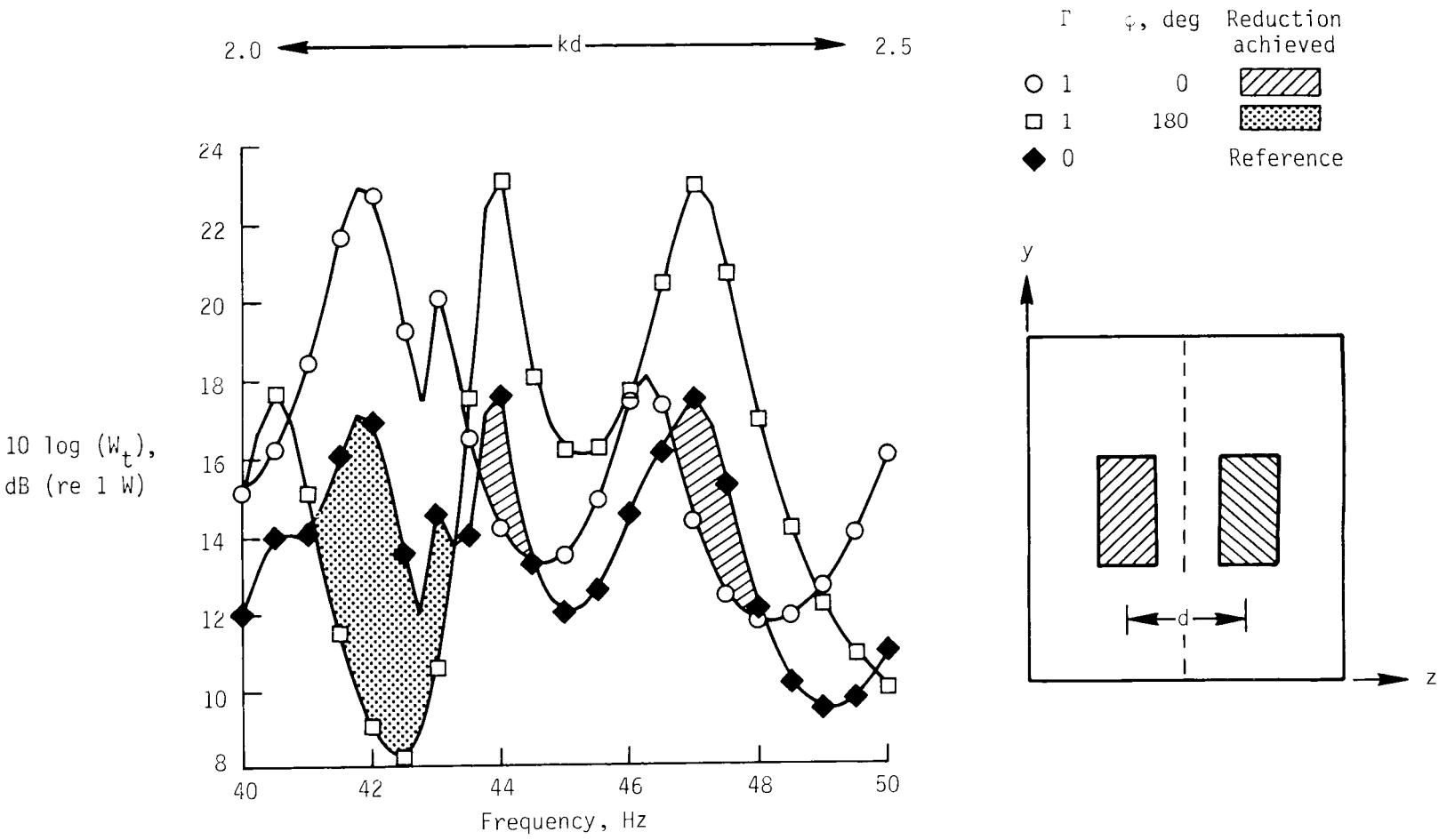

(b) $a = 1.3$ m: $2b = 2.7$ m: $d = 2$ source widths.

Figure 6. Continued.

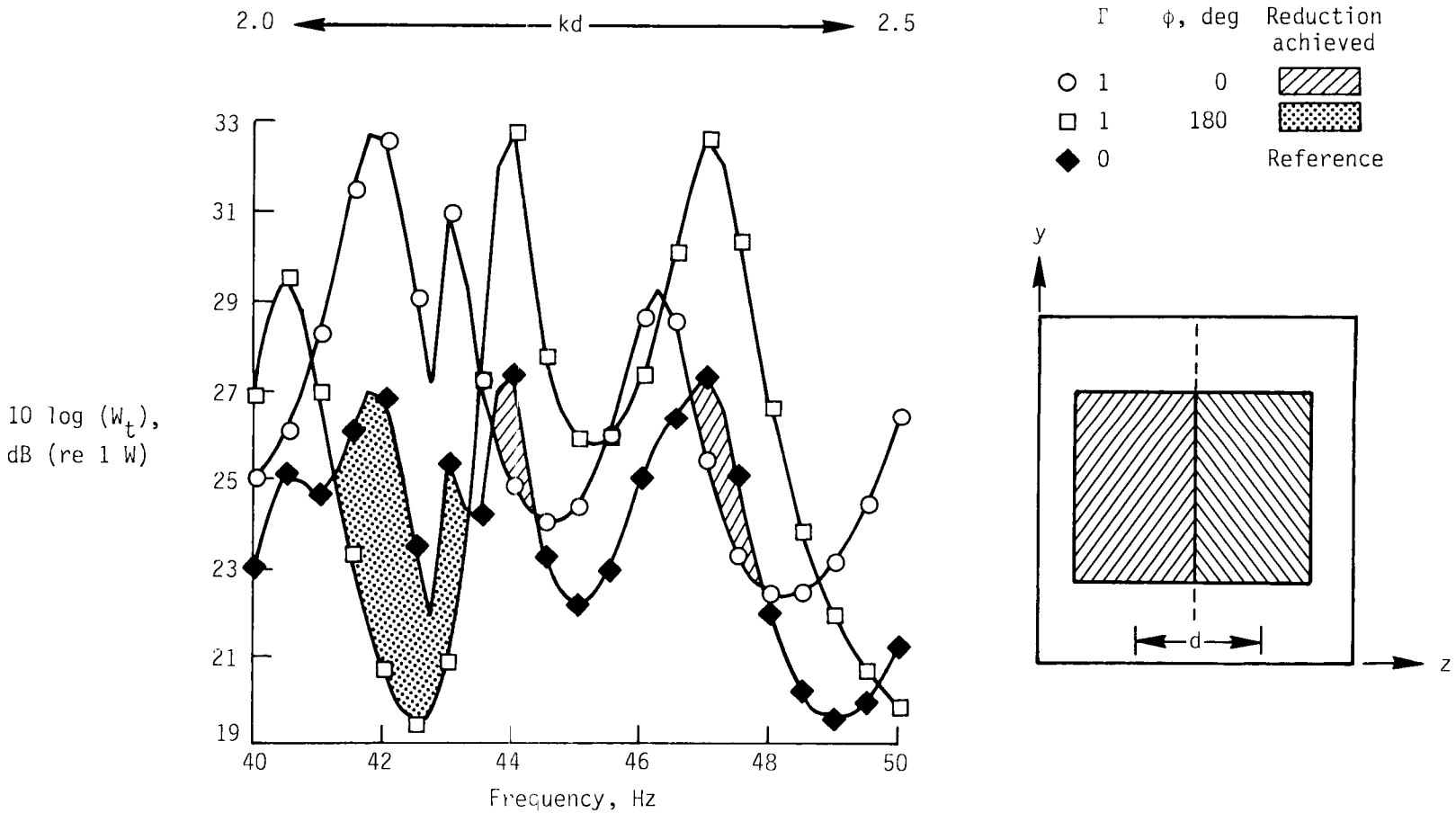

(c) $a = 2.7$ m; $2b = 5.3$ m; $d = 1$ source width.

Figure 6. Concluded.

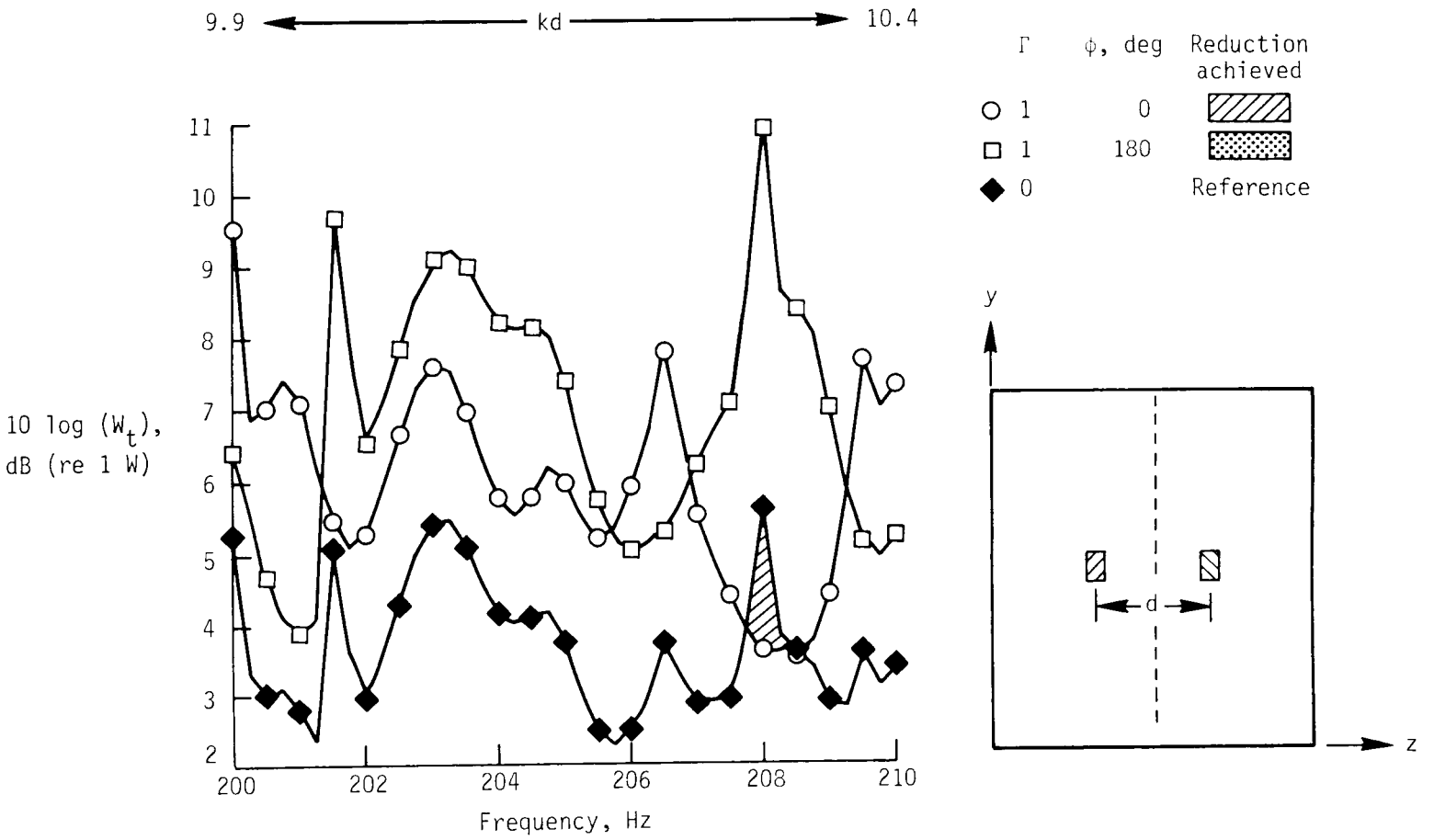

(a) $a = 0.3$ m: $2b = 0.6$ m: $d = 9$ source widths.

Figure 7. Effect of secondary source size on total power level, high frequency case. $\beta = 0.1$.

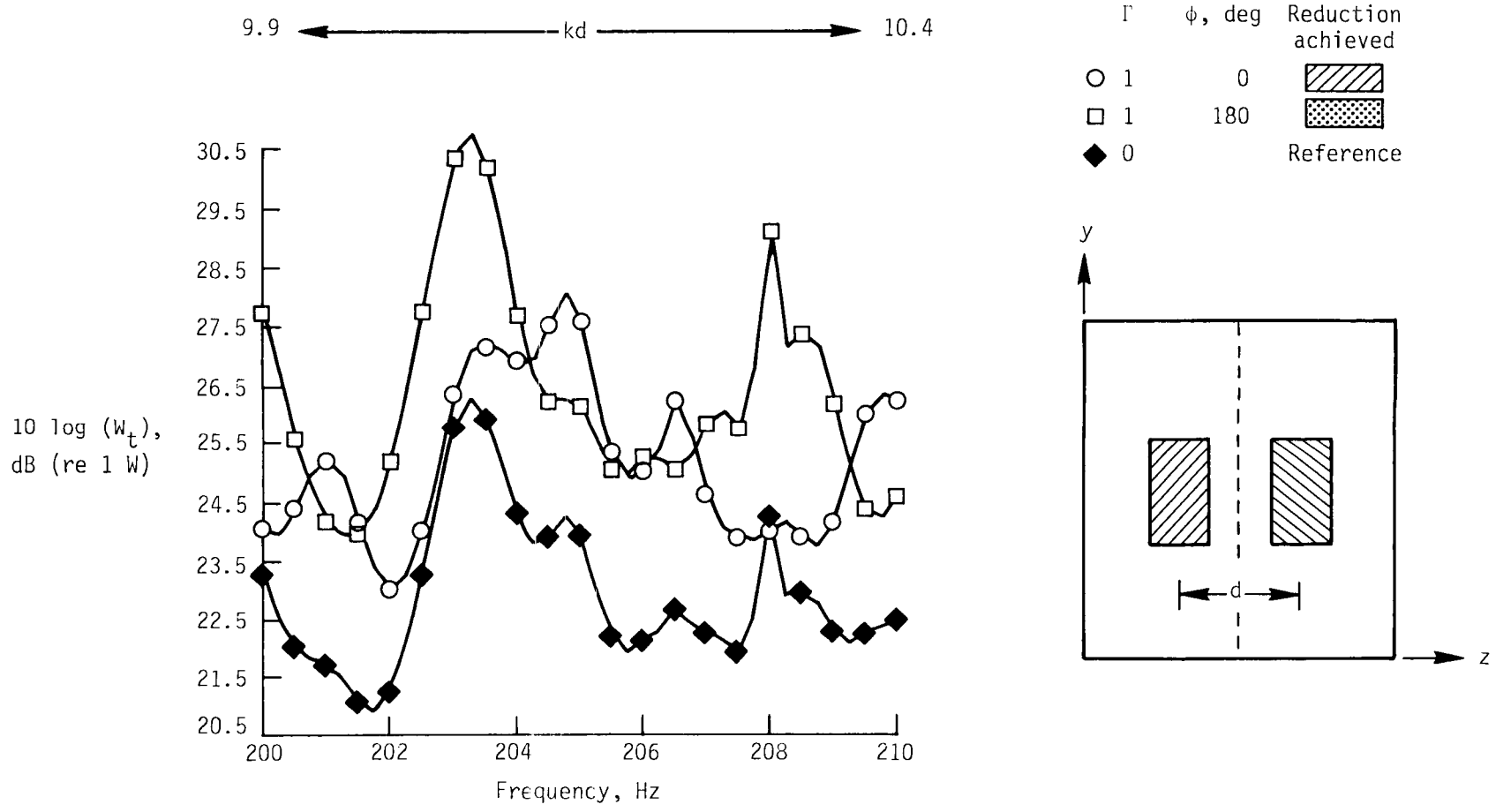

(b) $a = 1.3$ m; $2b = 2.7$ m; $d = 2$ source widths.

Figure 7. Continued.

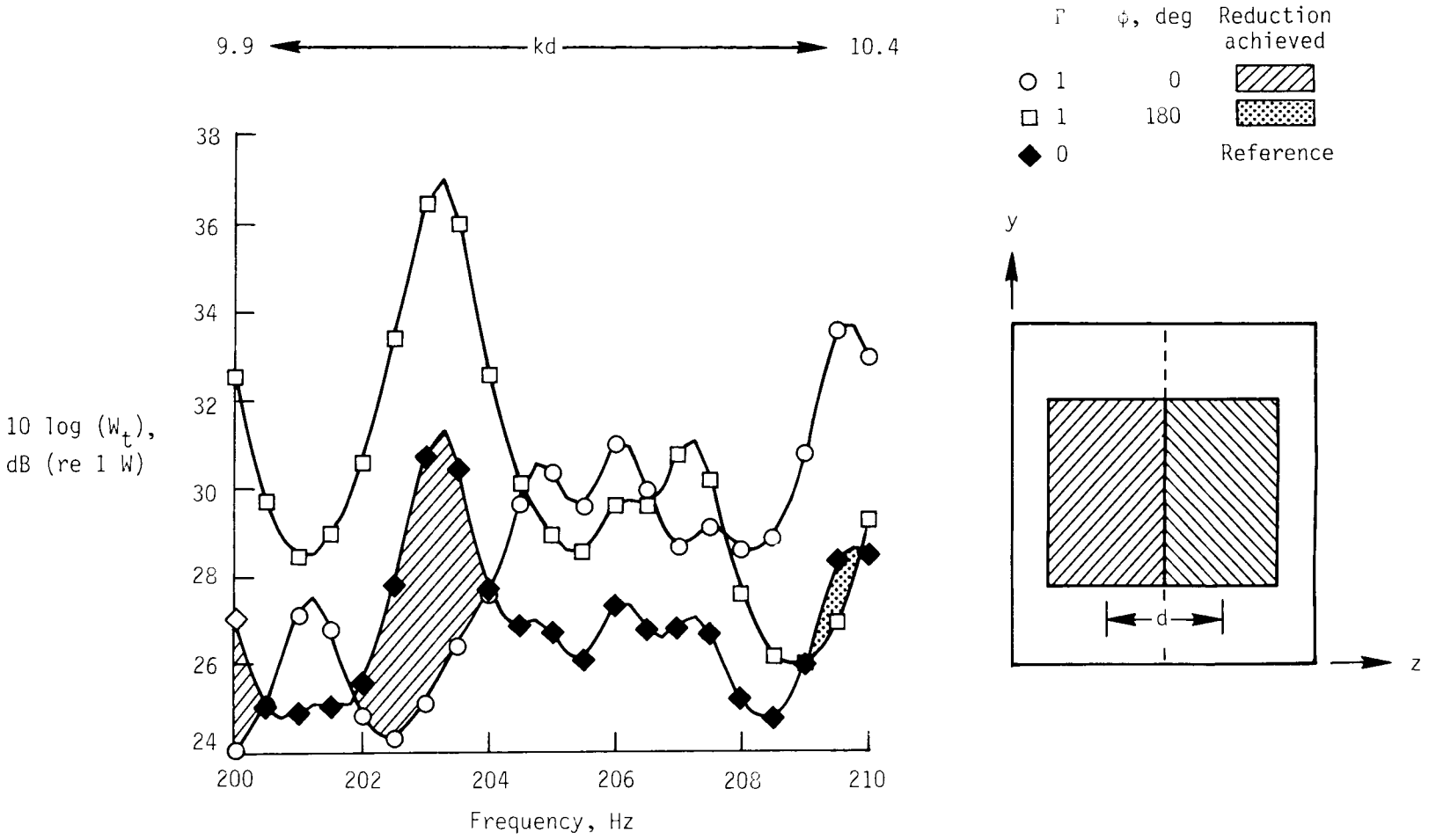

(c) $a = 2.7$ m: $2b = 5.3$ m: $d = 1$ source width.

Figure 7. Concluded.

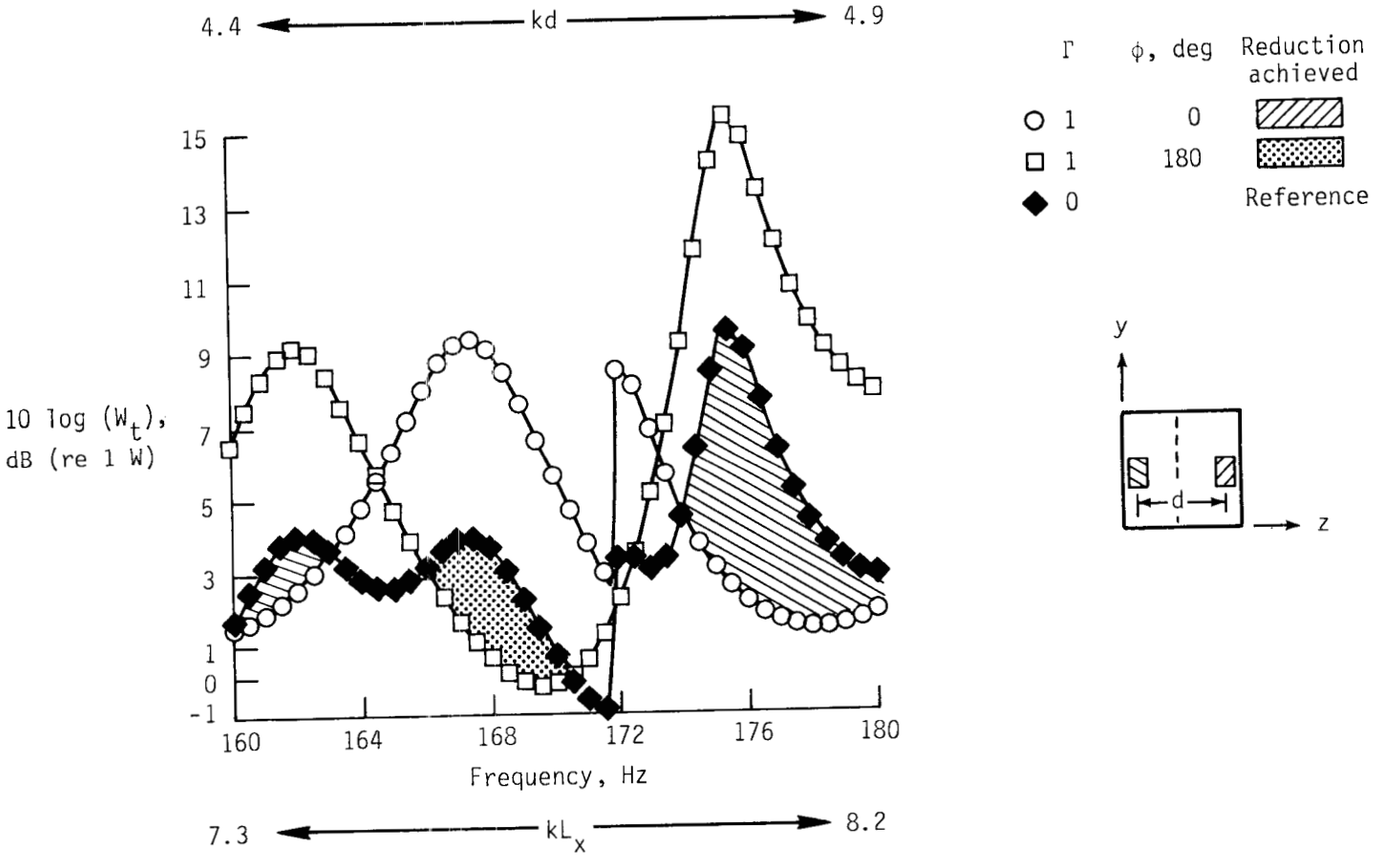

(a) $L_x = 2.5$ m; $L_y = 2.25$ m; $L_z = 2.0$ m.

Figure 8. Effect of enclosure size on total power level, 160–180 Hz. $\beta = 0.1$; $a = 0.3$ m; $2b = 0.6$ m; $d = 5$ source widths.

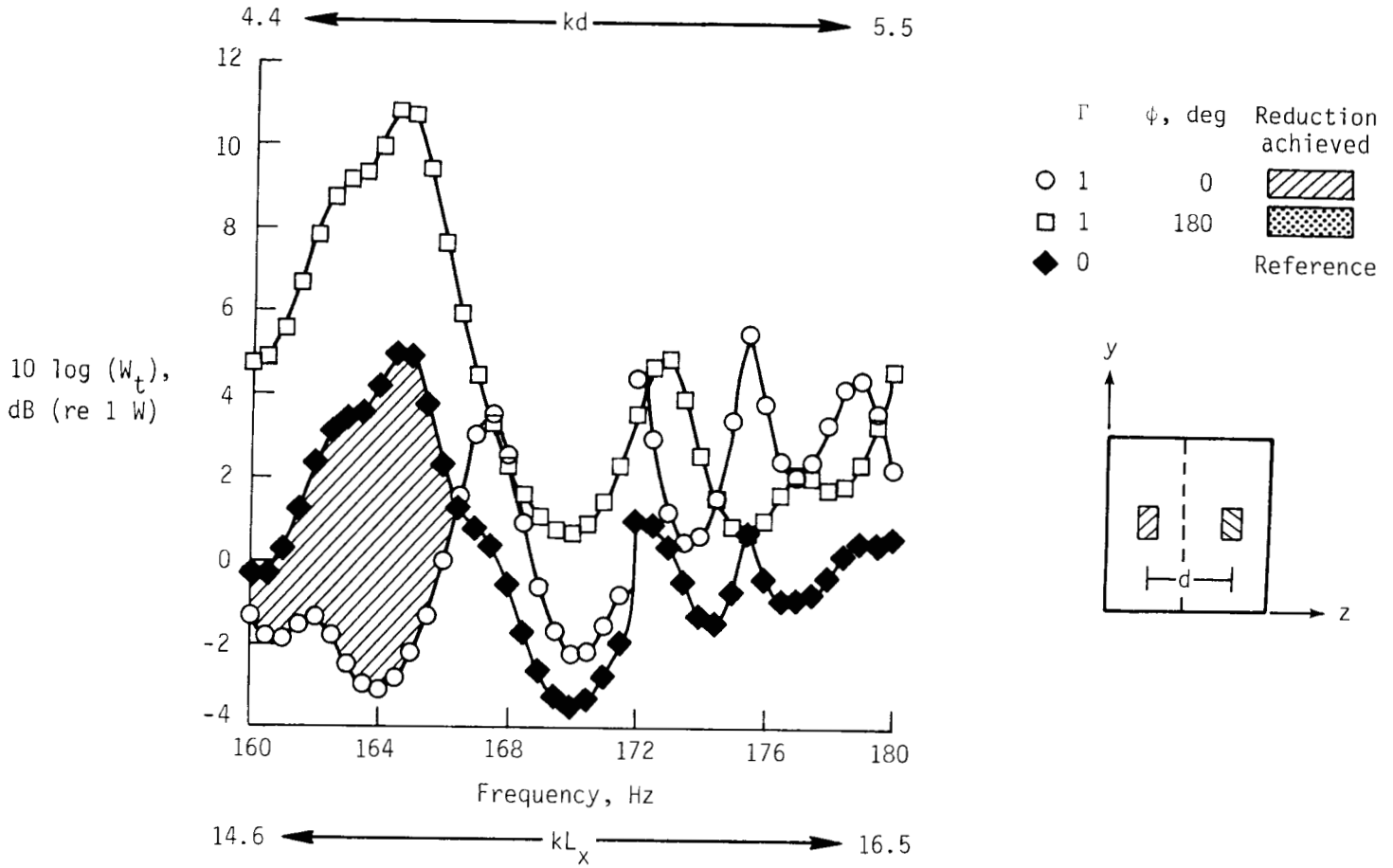

(b) $L_x = 5.0$ m; $L_y = 4.5$ m; $L_z = 4.0$ m.

Figure 8. Continued.

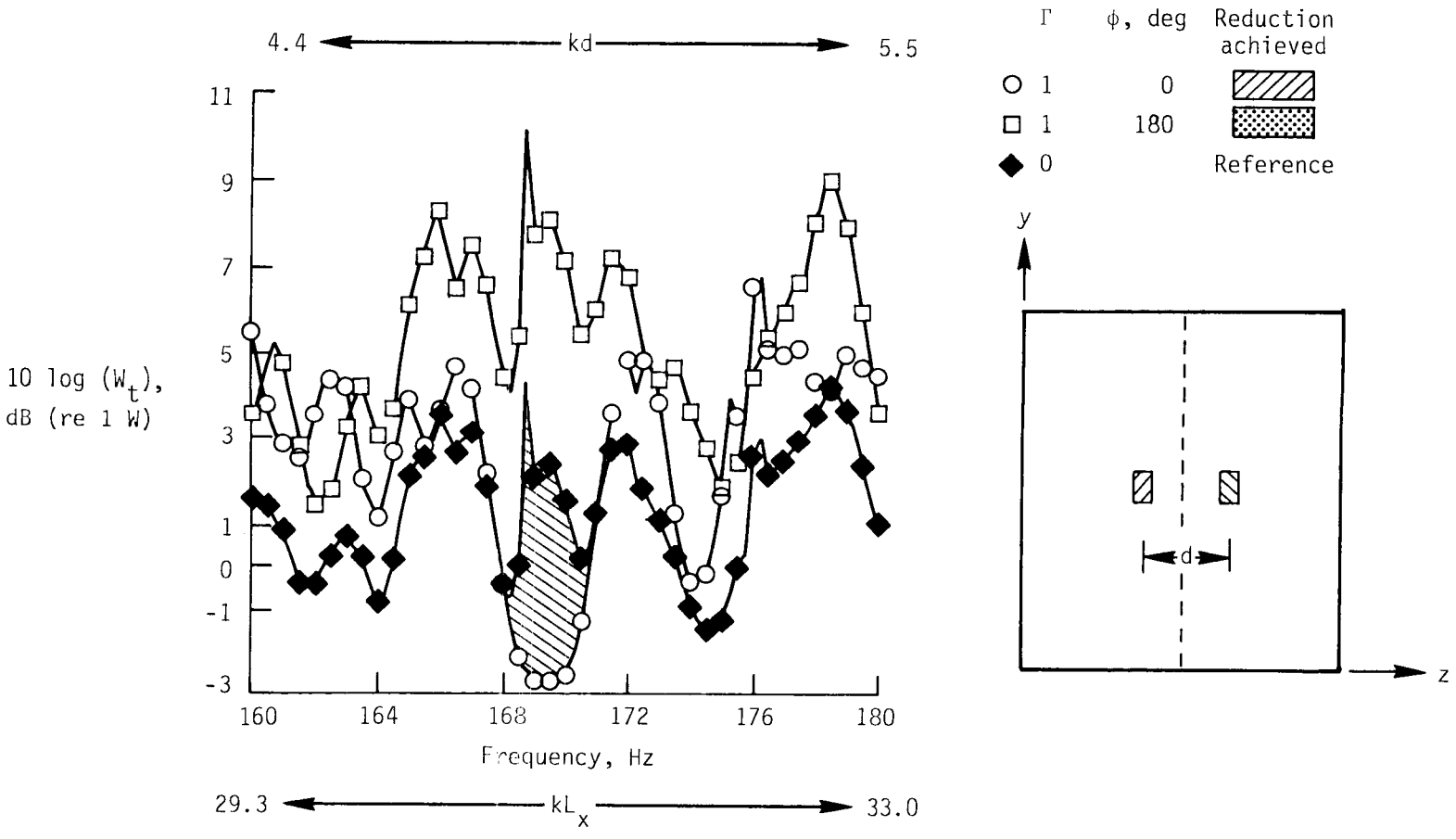

(c) $L_x = 10.0$ m; $L_y = 9.0$ m; $L_z = 8.0$ m.

Figure 8. Concluded.

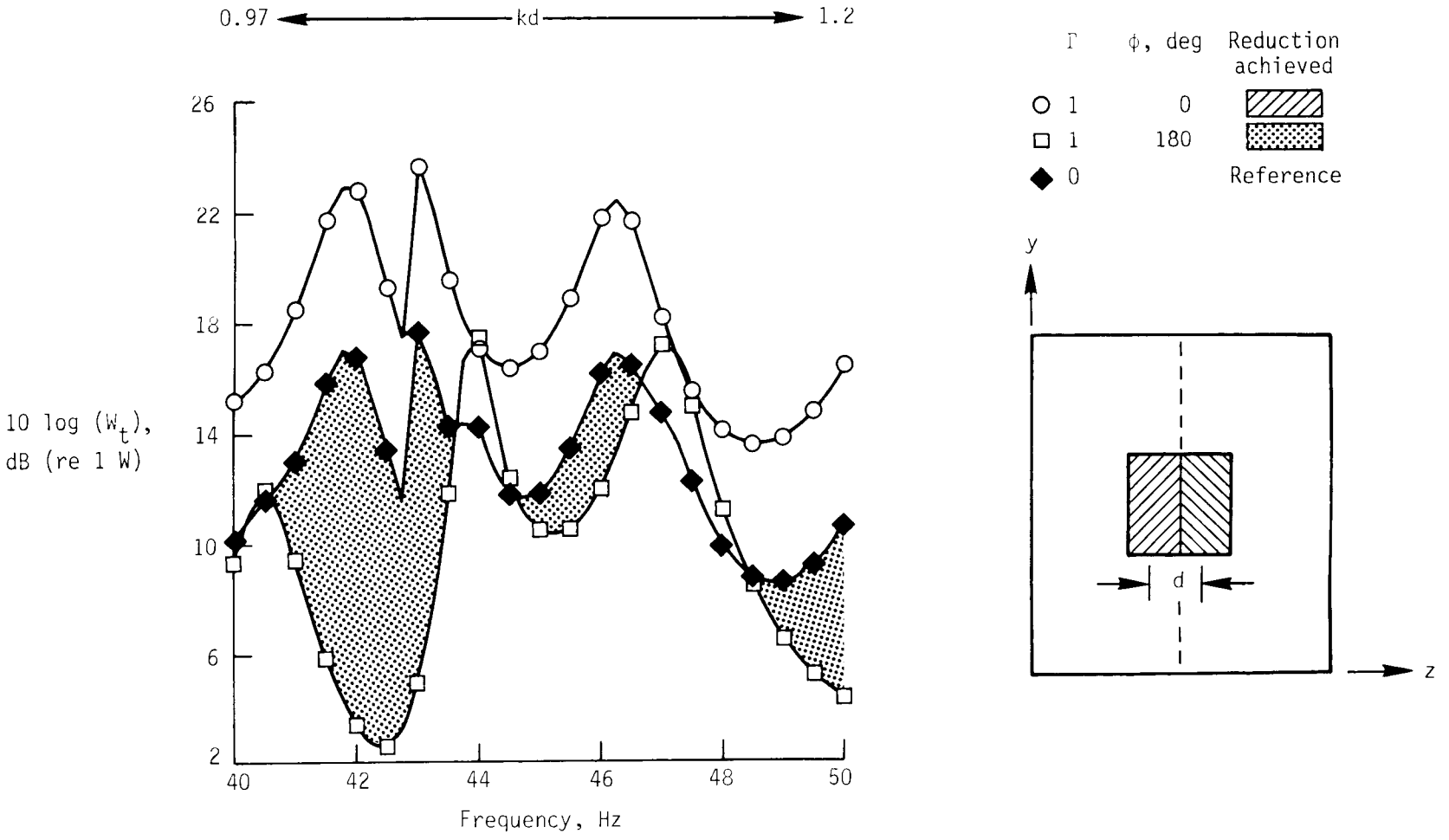

(a) $\beta = 0.1$.

Figure 9. Effect of wall admittance on total power level for closely spaced sources. low frequency case. $a = 1.3$ m: $b = 2.7$ m: $d = 1$ source width.

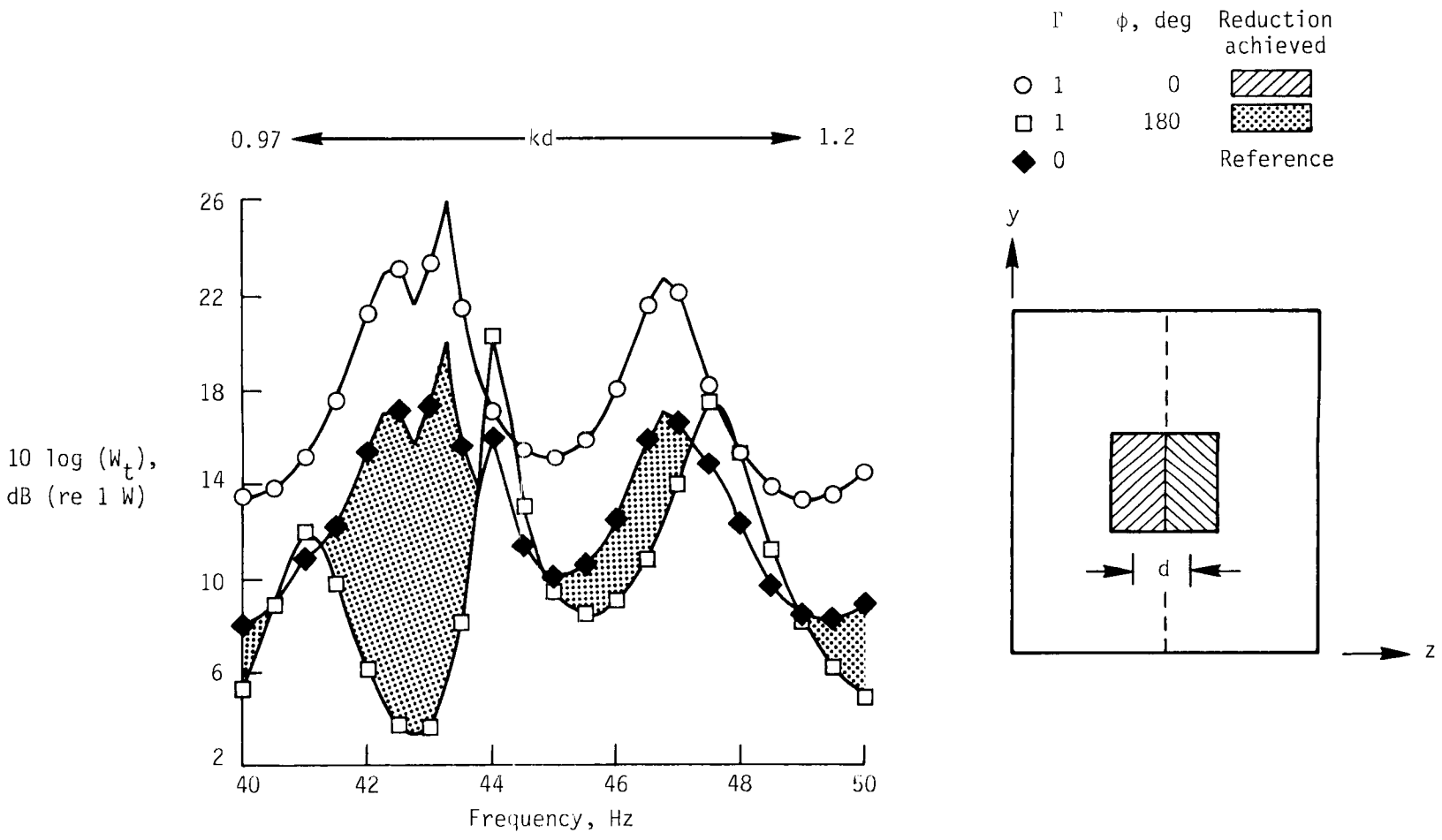

(b) $\beta = 0.1 + 0.1i$.

Figure 9. Continued.

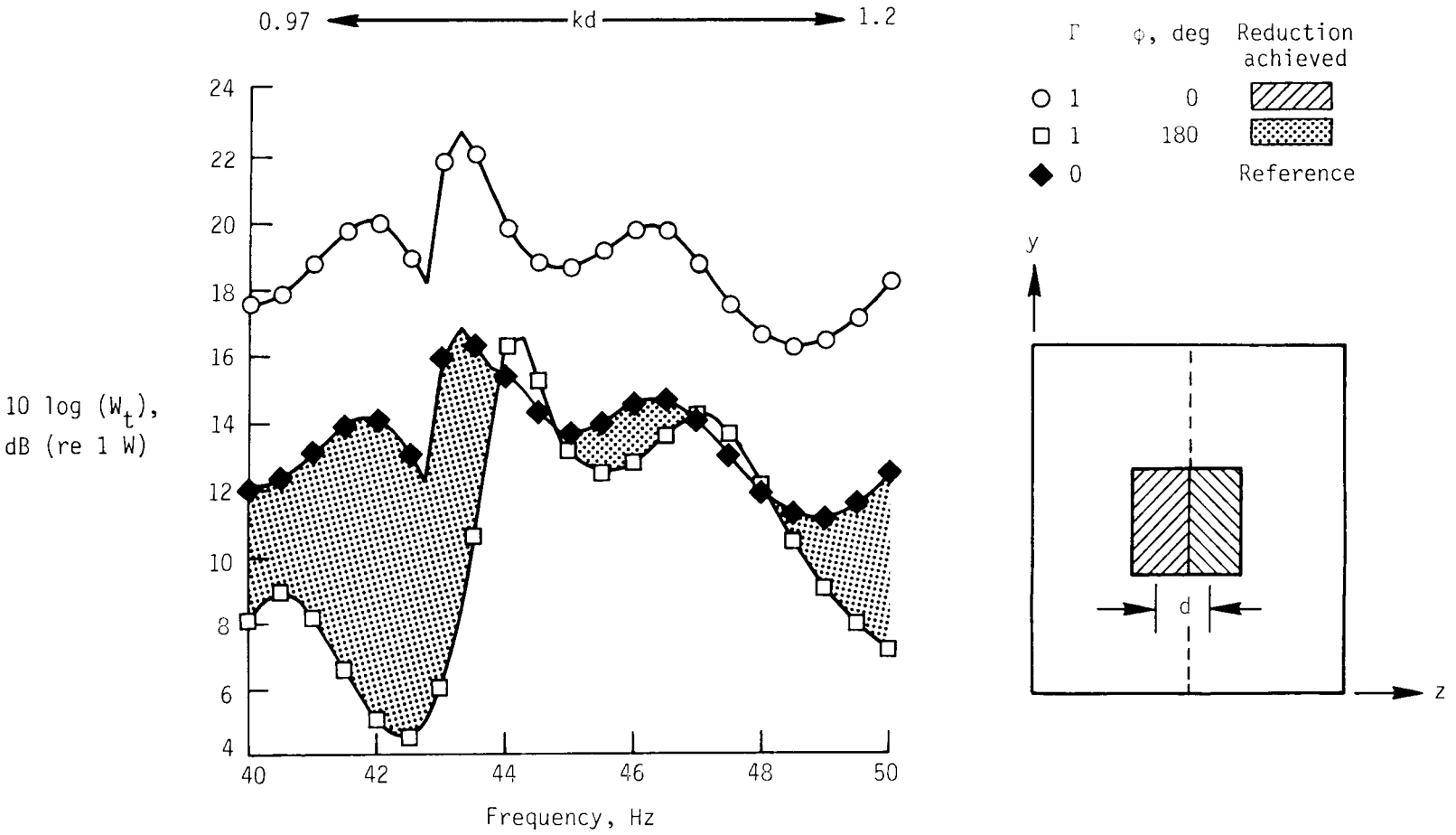

(c) $\beta = 0.2$.

Figure 9. Concluded.

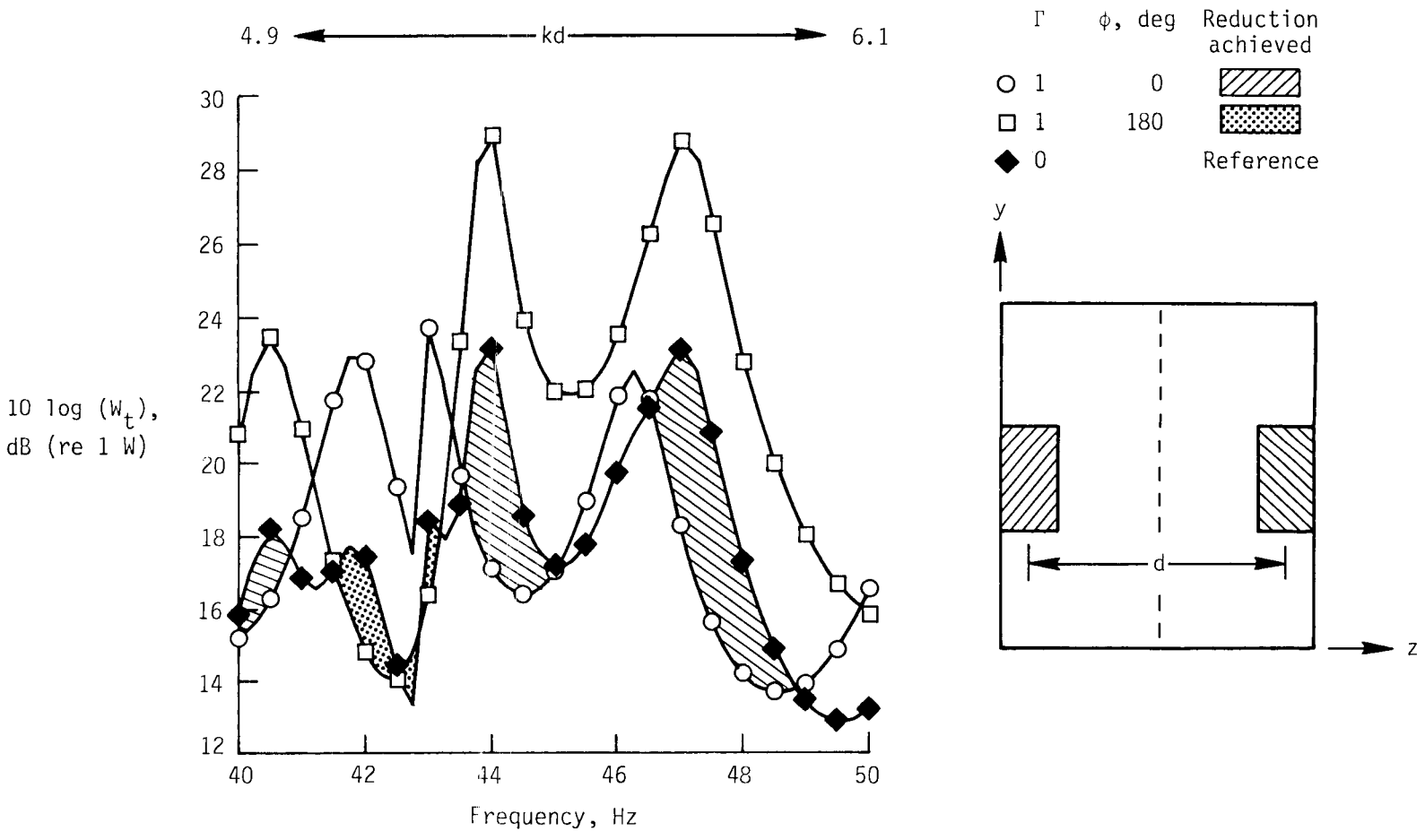

(a) $\beta = 0.1$.

Figure 10. Effect of wall admittance on total power level for widely spaced sources, low frequency case. $a = 1.3$ m; $b = 2.7$ m; $d = 5$ source widths.

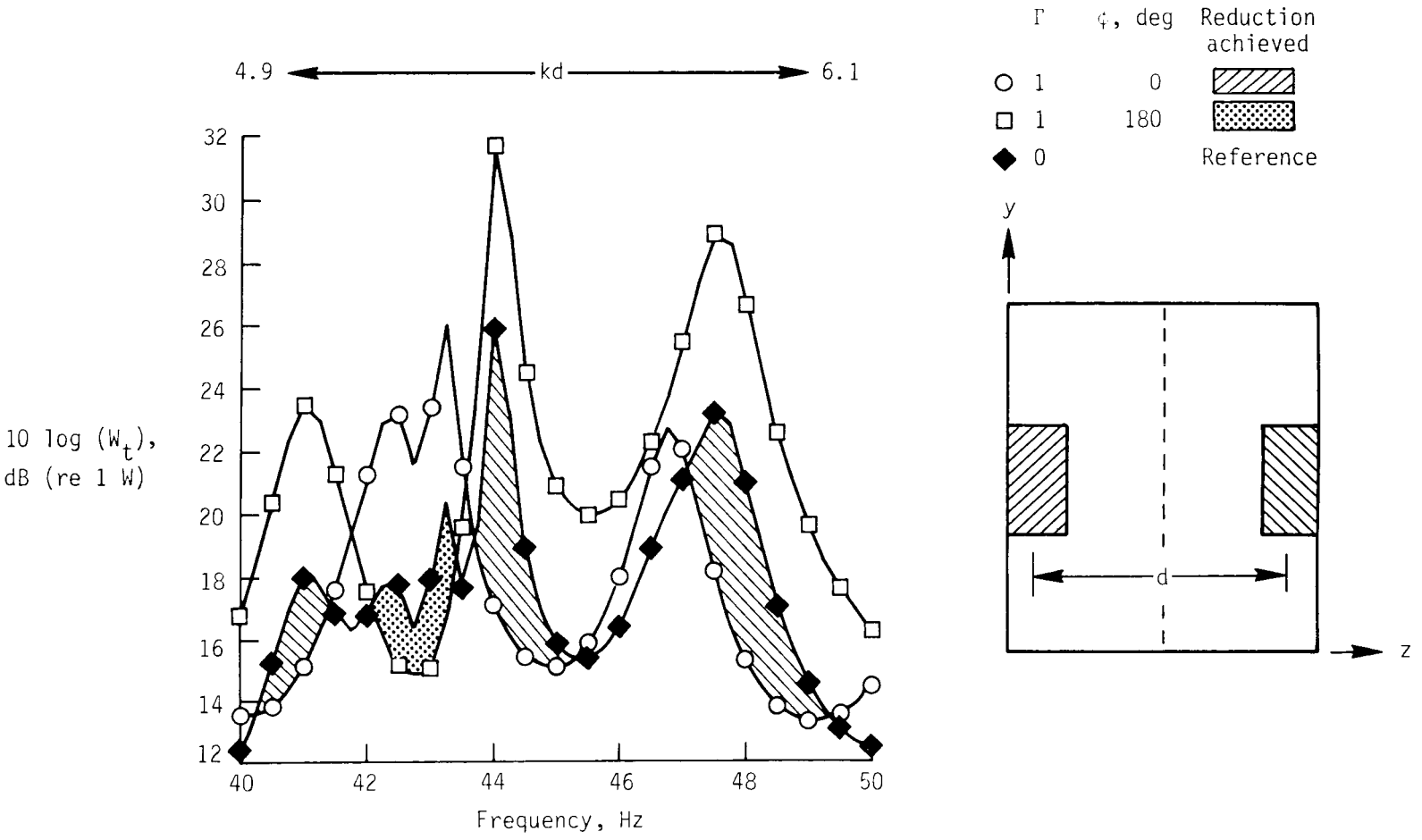

(b) $\beta = 0.1 + 0.1i$.

Figure 10. Continued.

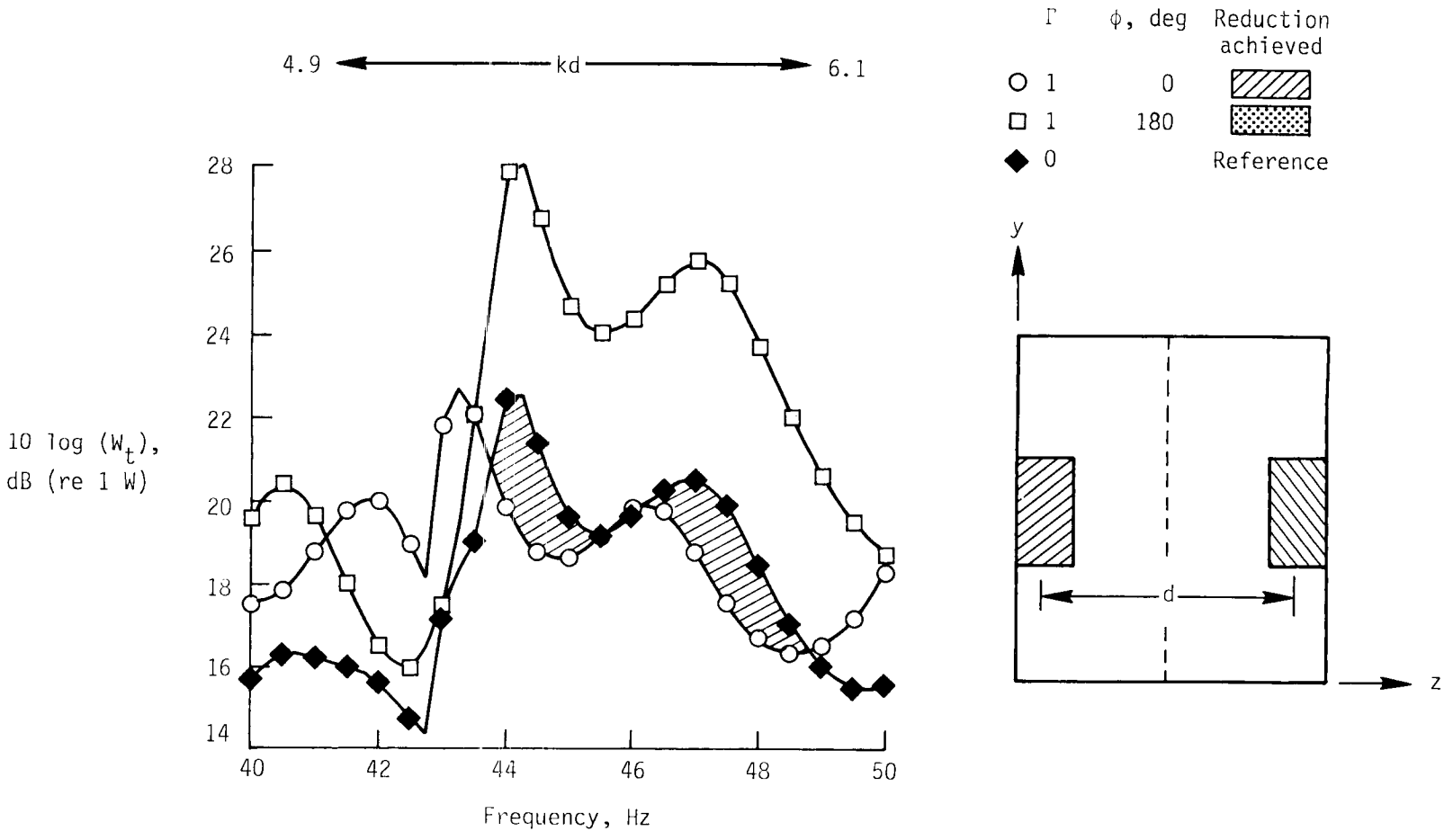

(c) $\beta = 0.2$.

Figure 10. Concluded.

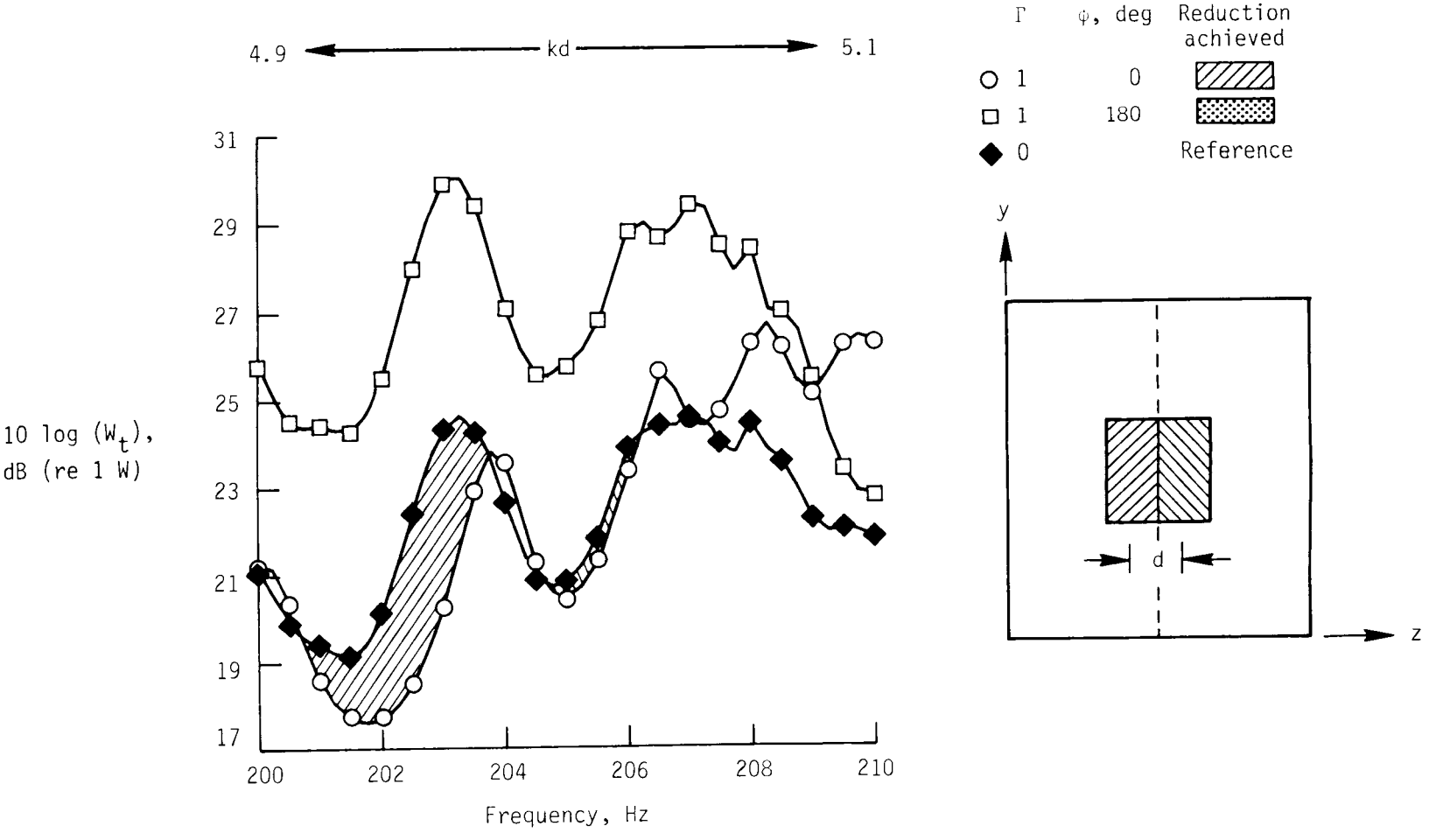

(a) $\beta = 0.1$.

Figure 11. Effect of wall admittance on total power level for closely spaced sources, high frequency case. $a = 1.3$ m; $b = 2.7$ m; $d = 1$ source width.

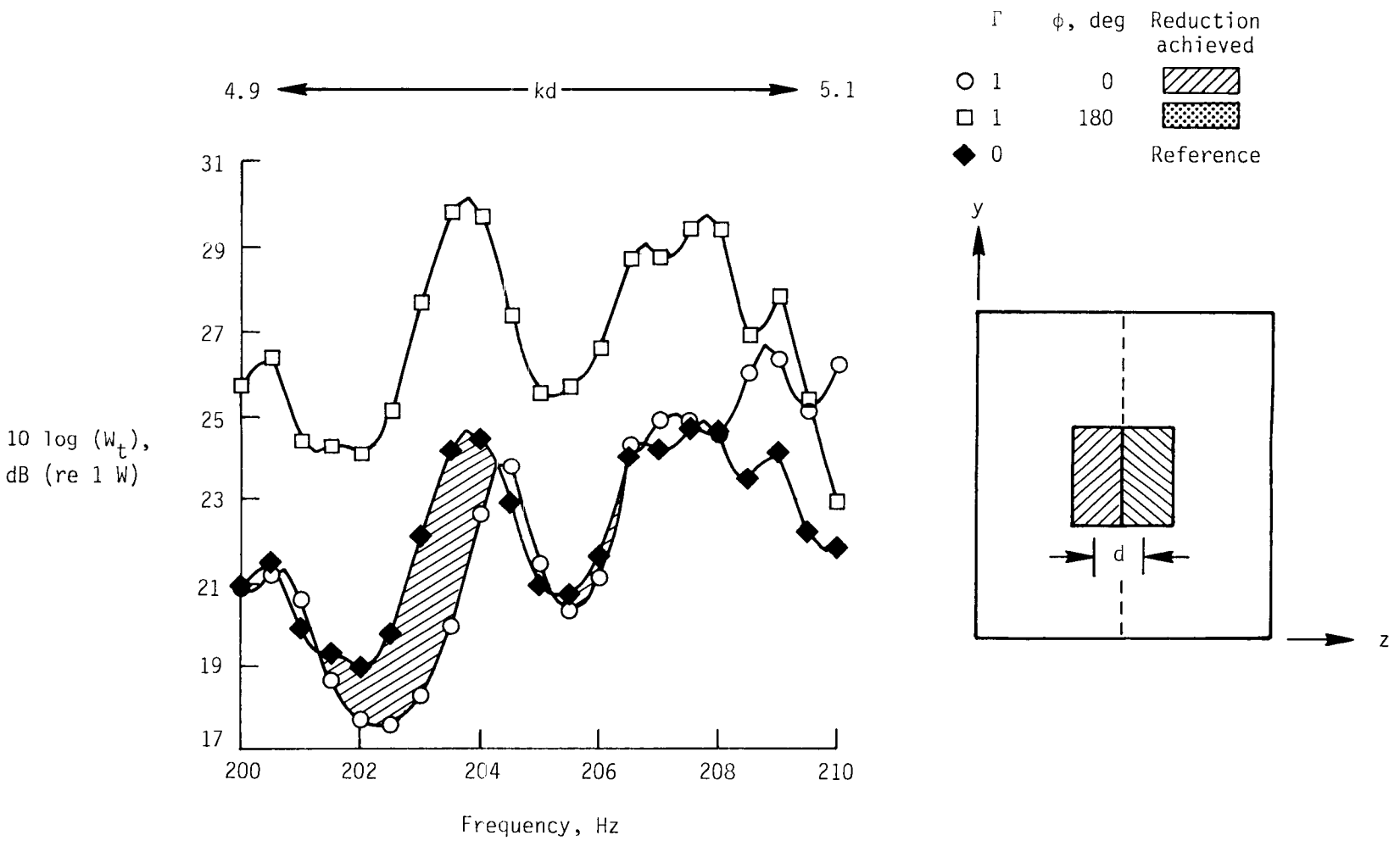

(b) $\beta = 0.1 + 0.1i$.

Figure 11. Continued.

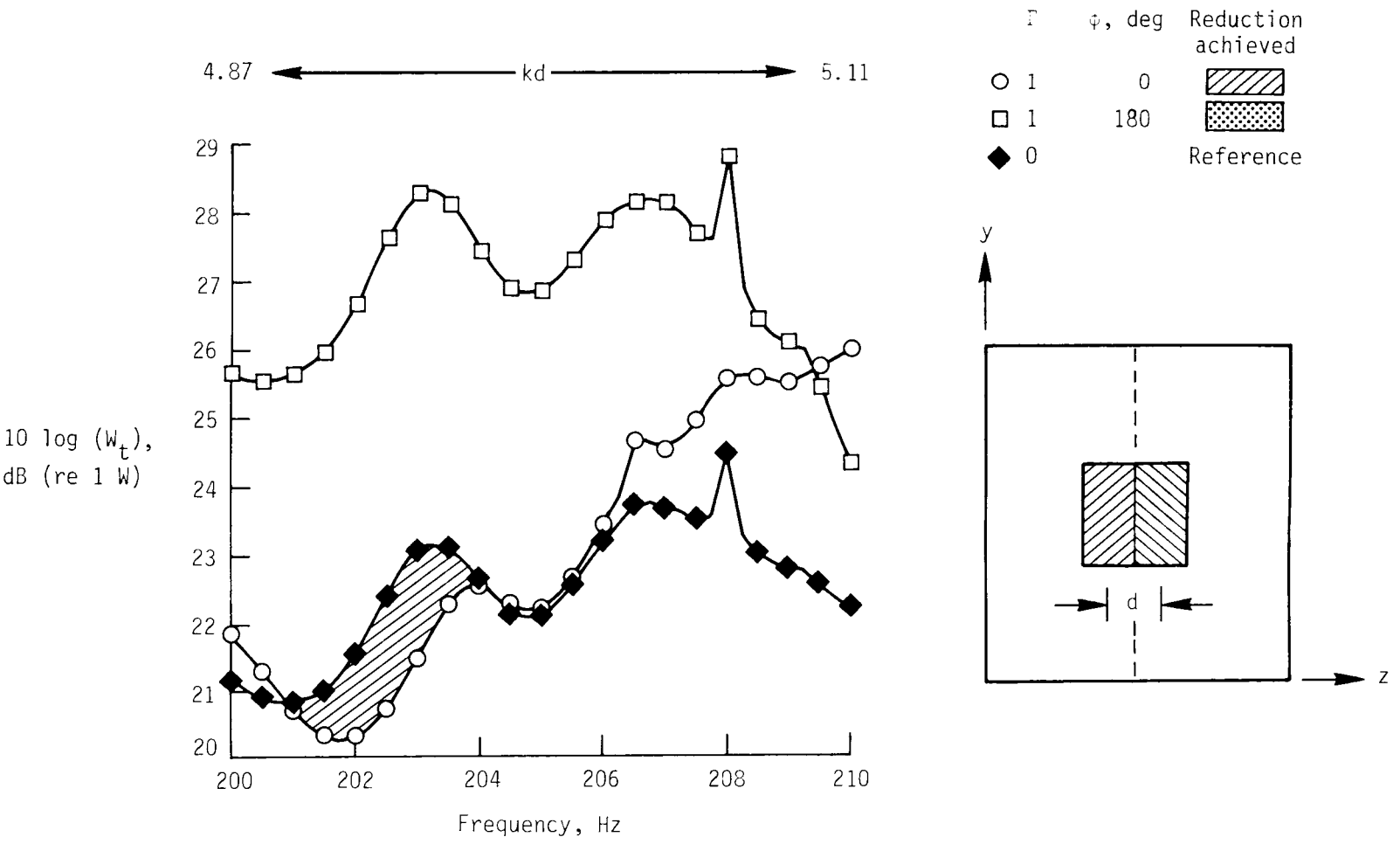

(c) $\beta = 0.2$.

Figure 11. Concluded.

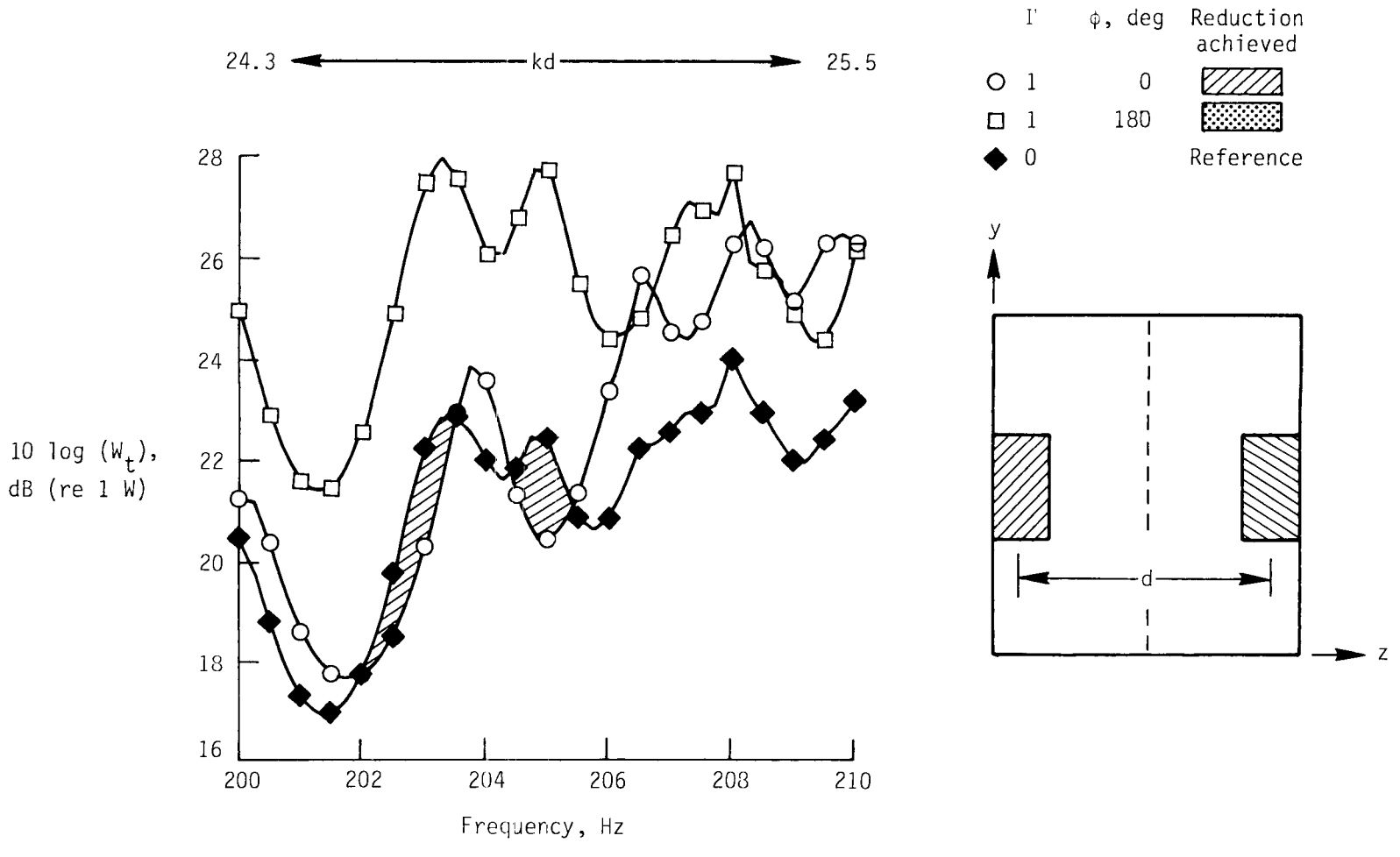

(a) $\beta = 0.1$.

Figure 12. Effect of wall admittance on total power level for widely spaced sources, high frequency case. $a = 1.3$ m; $b = 2.7$ m; $d = 5$ source widths.

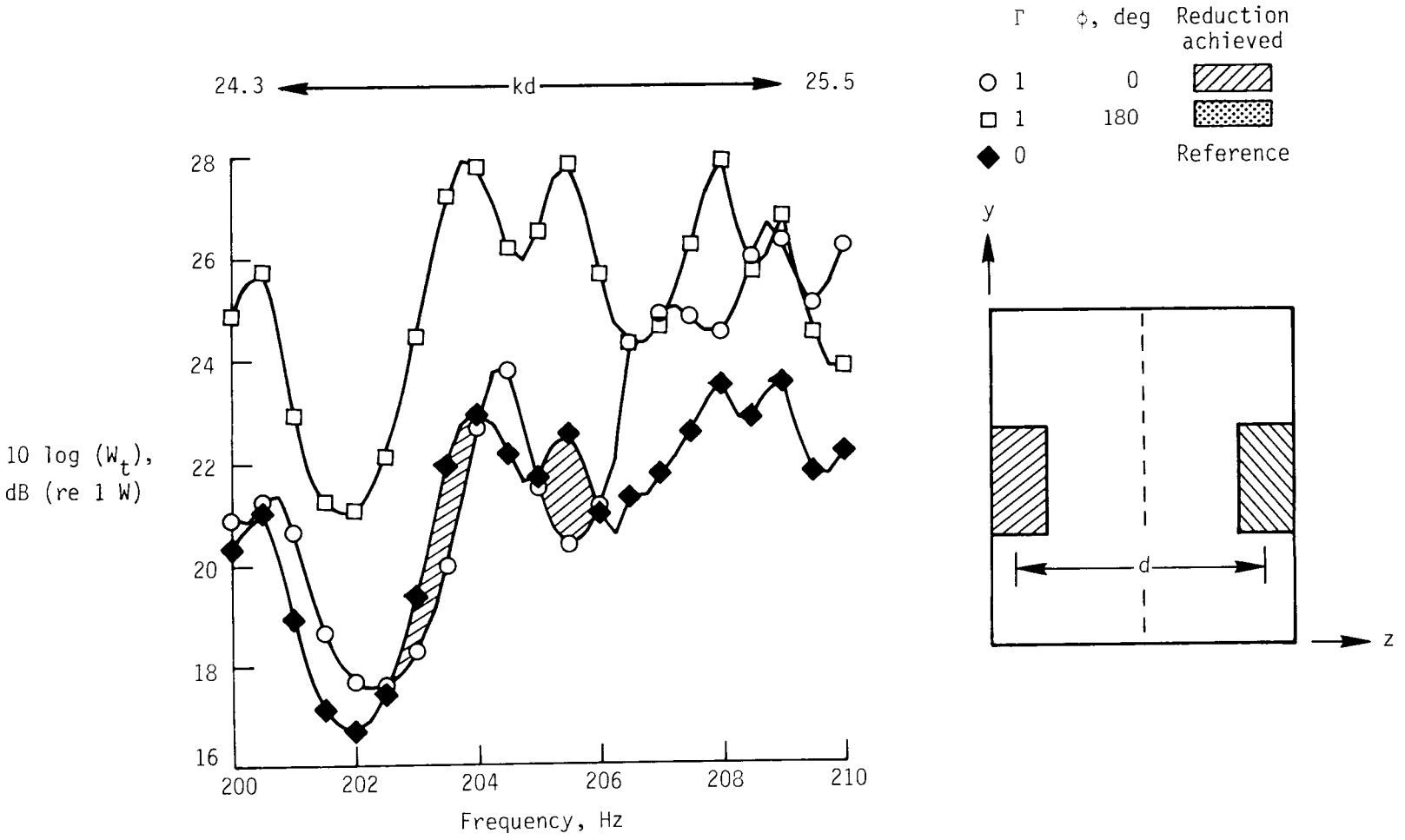

(b) $\beta = 0.1 + 0.1i$.

Figure 12. Continued.

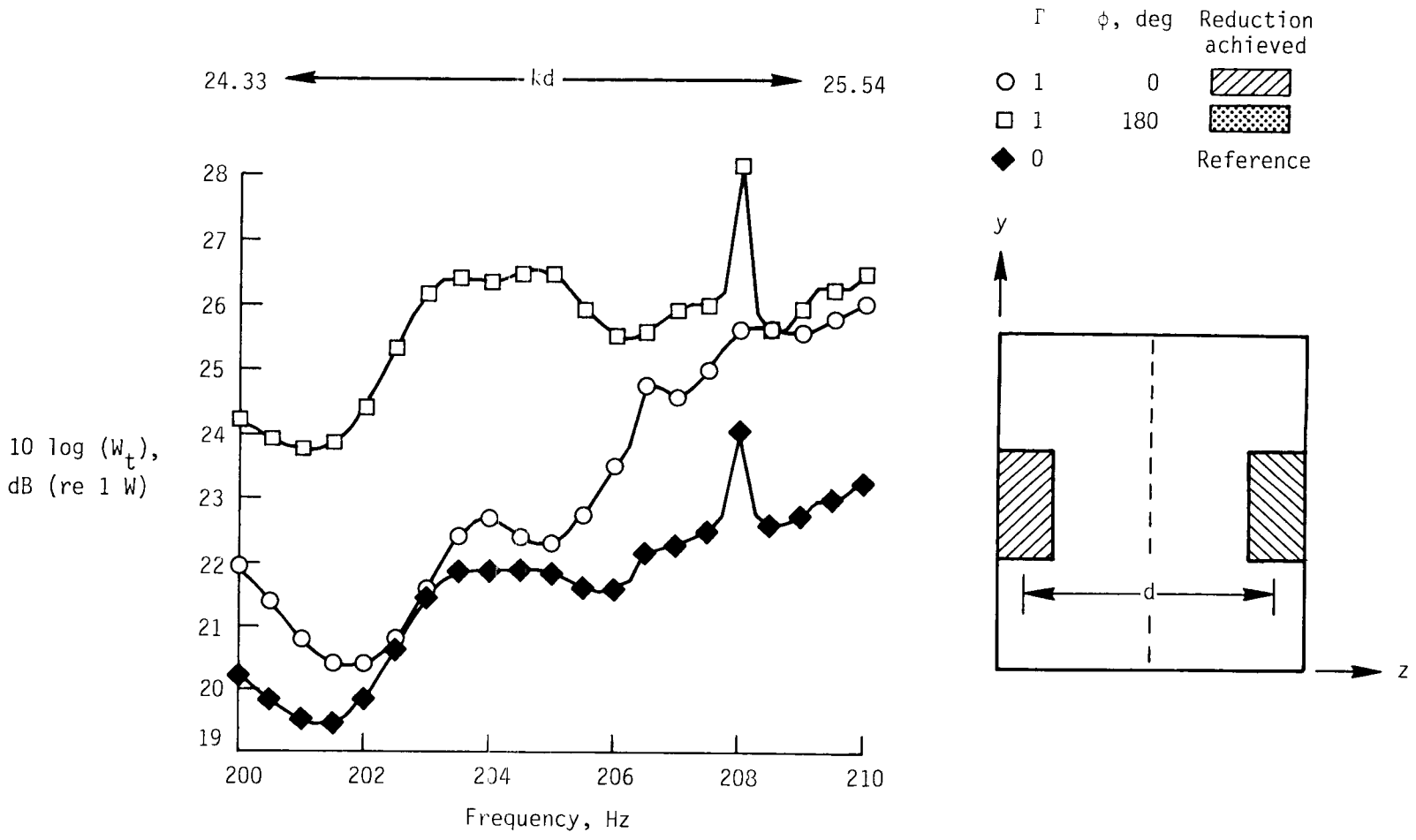

(c) $\beta = 0.2$.

Figure 12. Concluded.

1. Report No.	2. Government Accession No.	3. Recipient's Catalog No.
NASA TP-2472		

4. Title and Subtitle	5. Report Date
Analytical Study of Acoustic Response of a Semireverberant Enclosure With Application to Active Noise Control	December 1985
	6. Performing Organization Code: 505-33-90-02
7. Author(s): Tony L. Parrott, David B. Schein, and Doreen Gridley	8. Performing Organization Report No.: L-15944
9. Performing Organization Name and Address: NASA Langley Research Center, Hampton, VA 23665-5225	10. Work Unit No.
	11. Contract or Grant No.
12. Sponsoring Agency Name and Address: National Aeronautics and Space Administration, Washington, DC 20546-0001	13. Type of Report and Period Covered: Technical Paper
	14. Sponsoring Agency Code

15. Supplementary Notes

Tony L. Parrott: Langley Research Center, Hampton, Virginia.
David B. Schein: The George Washington University Joint Institute for Advancement of Flight Sciences, Hampton, Virginia, now with Northrop Corporation, Pico Rivera, California.
Doreen Gridley: U.S. Naval Avionics Center, Indianapolis, Indiana.

16. Abstract

The acoustic response of a semireverberant enclosure with two interacting, velocity-prescribed source distributions was analyzed using standard modal analysis techniques with a view toward a better understanding of active noise control. Different source and enclosure dimensions, source separations, and single-wall admittances were studied over representative frequency bandwidths of 10 Hz with source relative phase as a parameter. Results indicate that power radiated into the enclosure agrees qualitatively with the spatial average of the mean square pressure, even though the reverberant field is nondiffuse. Decreases in acoustic power can therefore be used to estimate global noise reduction in a nondiffuse semireverberant environment. As might be expected, parametric studies indicate that maximum power reductions of up to 25 dB can be achieved when secondary and primary sources are compact and closely spaced. Although less success is achieved with increasing frequency and source separation or size, significant suppression of up to 8 dB still occurs over the 1 to 2 Hz bandwidth.

17. Key Words (Suggested by Authors(s))	18. Distribution Statement
Active noise control Semireverberant enclosure Modal analysis Parametric study	Unclassified Unlimited Subject Category 71

19. Security Classif.(of this report)	20. Security Classif.(of this page)	21. No. of Pages	22. Price
Unclassified	Unclassified	46	A03

For sale by the National Technical Information Service, Springfield, Virginia 22161

National Aeronautics and
Space Administration
Code NIT-4

Washington, D.C.
20546-0001

3 2 U.A, 881122 S001b1DSR
DEPT OF THE AIR FORCE
ARNOLD ENG DEVELOPMENT CENTER(AFSC)
ATTN: LIBRARY/DOCUMENTS
ARNOLD AF STA TN 37389

NASA